Available online at www.sciencedirect.com
ScienceDirect
Comput. Methods Appl. Mech. Engrg. 368 (2020) 113182
Computer methods in applied mechanics and engineering
www.elsevier.com/locate/cma

A variational multiscale framework for atmospheric turbulent flows over complex environmental terrains

M. Ravensbergen[a], T.A. Helgedagsrud[b], Y. Bazilevs[c], A. Korobenko[a,*]

[a] *Department of Mechanical and Manufacturing Engineering, University of Calgary, Calgary, AB, T2N 1N4, Canada*
[b] *Department of Structural Engineering, Norwegian University of Science and Technology, Richard Birkelands v 1a, Trondheim NO-7491, Norway*
[c] *School of Engineering, Brown University, 184 Hope St., Providence, RI 02912, USA*

Received 25 March 2020; received in revised form 22 May 2020; accepted 23 May 2020
Available online 6 June 2020

Abstract

A residual-based variational multi-scale (VMS) modeling framework is applied to simulate atmospheric flow over complex environmental terrains. The VMS framework is verified and validated using two test cases using linear finite element (FEM) and quadratic non-uniform rational B-spline (NURBS) discretizations. First, the flow over the 3D, axisymmetric Gaussian hill (normally distributed surface) is used to compare the results with FEM and NURBS discretization. Next, the actual terrain of the Bolund hill is used to demonstrate the efficacy of the framework. Good agreement with published data, coming from simulations and field measurements, is achieved, with the NURBS discretization showing much better per-degree-of-freedom accuracy compared with linear FEM. The paper includes a comprehensive review of experimental and numerical methods, and the corresponding challenges, for complex-terrain flows, which provides a proper context for the developments presented in this work.

Keywords: CFD; Complex terrain; FEM; VMS; NURBS; IGA

1. Introduction

Wind energy is a growing renewable source of electricity generation as the world combats climate change. How to deal with complex (mountainous or hilly) terrains is a major knowledge gap in wind energy. In such terrains, the wind speed and direction are highly variable based on location. Accurate, site specific prediction of environmental flow over complex terrain is necessary to predict aerodynamic loading, which, in turn, determines the annual energy production and turbine lifespan [1–4]. Although wind energy is the primary application for the present work, accurate prediction of local flow fields in complex terrains has numerous other engineering applications. These include the design of tall buildings, long-span bridges, electrical transmission lines, and antenna towers [2,5,6]; natural building ventilation and pedestrian wind comfort [7]; airport, power plant, and industrial project siting [8]; pollutant dispersion [9–14]; soil erosion for agriculture and forestry [5,15–17]; and ship maneuvering in harbors [18].

* Corresponding author.
E-mail address: artem.korobenko@ucalgary.ca (A. Korobenko).

https://doi.org/10.1016/j.cma.2020.113182

1.1. Review of experimental and numerical approaches for complex-terrain flows

Full scale experimental field studies give the most accurate description of the flow to understand the physical phenomenon. Some early experimental campaigns from different areas in Scotland in the late 1970s and early 1980s are Askervein Hill [19], Ailsa Craig Island [16], and Blashaval hill [20]. Bradley [5] looked at flow over Black Mountain, a broad hill with uniform slope in Australia. All these cases studied relatively isolated hills with relatively gentle slopes of less than 30 degrees and measured wind speed upstream and downstream of the feature using fixed anemometers. Taylor et al. [21] review and categorize some of the most important field studies from this era. Sampling concentration of a source dispersed from upstream can also provide insight. Lavery et al. [22] examined dispersion around Cinder Cone Butte in Idaho. Later, Ryan et al. [23] examined dispersion of a sample released upstream of Steptoe Butte in Washington state.

Recent field studies include more complex topography. Two coastal examples are Ria de Ferrol in Spain, a narrow harbor surrounded by hills and valleys instrumented with five ultrasonic anemometers [18] and the cliffs on the island of Madeira [3]. In the later, the use of a sonic anemometer revealed that some locations under consideration for a wind turbine were in highly turbulent re-circulation regions with reversed flow. The Askervein hill has long been the most commonly used field campaign for model validation. However since Askervein has a generally 2-D geometry and steepness less than 20 degrees, it may not represent a complex enough test case for validation [24]. As an alternative, the Bolund hill experiment [25,26] was conducted for the express purpose of validating complex terrain models. The topography features a 10 m high cliff facing the incoming wind, resulting in a large region of separated flow which is difficult for low fidelity modeling techniques to capture. Flow statistics in the Bolund hill experiment are measured at 10 different mast locations by sonic anemometers. Another recent experiment comes from the New European Wind Atlas near Perdigão in Portugal. The terrain consists of two steep parallel ridges about 1.5 km apart, 4 km long, and 500 m tall, and instrumented with over 50 meterological towers up to 100 m in height and several scanning lidars [27].

Although field studies provide the most accurate information, they are expensive and time consuming. A cheaper, faster alternative that can still provide accurate insights into the underlying physical phenomena are wind tunnel experiments. Wind tunnel experiments on idealized geometries are simpler than measuring wind profiles in the field, and more data can be collected. One early experiment often used for validation is the RUSHIL case with 3 hills of varying steepness [28]. Britter et al. [29] performed a wind tunnel experiment to examine the physical effects that occur within the boundary layer in the presence of hills. Gaussian (i.e. normally distributed) surfaces are a common test case for wind tunnel experiments [30]. Another common test case is a terrain with a sinusoidal profile in the streamwise direction such as the experiment of [31] where turbulent boundary layer flow is measured on slopes up to 0.5 for two different surface roughness values. Ayotte and Hughes [32] later measured flow over a single sinusoidal ridge with varying surface roughnesses and slopes. Wind tunnel experiments have also been performed on scale models of real topography such as the Askervein hill [33] and Bolund hill [34].

While on-site wind measurements can be more accurate, numerical models are frequently used. Modeling can supplement experiments by filling gaps between measurement locations, allow investigation into effects of changing parameters, and greatly reduce the cost and time requirement to evaluate a location. Both measurement campaigns in real topography and idealized surfaces in wind tunnels are useful for validating models for flow over complex terrain. Early computational models were based on linearized equations of motion. Field experiments of isolated hill with shallow slopes (e.g. [5,16,19,20]) helped to validate the analytical linear theories such as the one introduced by Jackson and Hunt [35]. The model of Jackson and Hunt separates the flow into an inner layer, where local shear stress perturbations from the terrain are significant, and an outer layer where they are not. The model solves a linearized form of the governing Navier–Stokes equations, and has formed the basis for many subsequent linear flow models. Such linear models perform better for terrains with gentle slopes (less than 0.2 [36]), with the linearization of the governing equations contributing to error on stepper terrains [3,37,38].

Fully non-linear, 3D, computational fluid dynamics (CFD) has potential to accurately model more complex terrain with steep slopes and sharp angles [18,38–40] as it is capable of including effects such as flow separation through the non-linear terms. CFD on complex terrain began primarily with Reynolds Averaged Navier–Stokes (RANS) solvers. Early examples of RANS solvers being used for complex terrain cases include Hewer [41] who modeled

flow over the Blashaval hill, Kim et al. [8] who compared different RANS models for the Cooper's ridge, Kettles hill, Askervein hill, and Sirhowy valley cases, and Castro et al. [42] who simulated the Askervein hill case. These RANS models are typically compared with results of linear flow theory models and in general researchers found that their RANS computations were better able to predict fluid velocities than linear models when comparing both models to measured velocities. RANS has also been applied to the kind of idealized geometry that is often tested in wind tunnel experiments, such as a Gaussian hill [43,44], the geometry from the RUSHIL experiment [45,46], and a sinusoidal hill [47]. More recently steady-state RANS solvers have been applied to large, more complex domains, often with reasonable results except locally in areas with large flow separation or re-circulation zones (see e.g. [3,18,24,38,40,48]). Blocken et al. [18] simulated the Ria de Ferrol, Spain experiment using 3D steady RANS with $k-\epsilon$ model and obtained the simulation results deviating by 10%–20% from measurements depending on grid quality, resolution and surface roughness parameterization.

Large eddy simulation (LES) is fundamentally superior to RANS in its ability to capture complex features in turbulent flows over highly complex terrains [2]. The increase in fidelity comes with an increased computational cost, however, recent advances in computing power have made LES solvers more popular for meso-scale studies such as validation against wind tunnel experiments. Some examples include the RUSHIL case [28], which was modeled using LES by [46] and the sinusoidal hill experiment of Gong et al. [31] which was simulated to investigate various sub-grid scale turbulence closures and stratified flow models [49,50]. Flow over a Gaussian hill was modeled with by LES by [51]. The Askervein hill case has also been considered using LES [52] and hybrid RANS/LES techniques [53]. Until recently, 3D steady RANS remained the main CFD approach for large areas of complex terrain. Blocken et al. [18] attribute this to two reasons, the first being the increased computational cost and the second being the lack of validation studies and best practice guidelines for cases of complex terrain beyond a single isolated hill. Additional challenges for LES were highlighted in the blind model comparison for the Bolund hill [39], where several RANS models predicted velocities and turbulence levels closer to the measured values than the LES models. LES is nevertheless becoming more popular and following the blind study Chaudhari [46] used LES to simulate flow over the Bolund hill with relatively good agreement compared to other modeling attempts. Recently, LES has been successfully applied to larger areas of complex terrain as well, such as the Perdigão region of two parallel ridges [54,55] and the Sierra Madre wind turbine site [56]. Correctly defining inlet conditions will continue to be a challenge for these very complex regions which do not have a well defined inflow region, but modelers have shown the ability for LES to reproduce at least the main characteristics of the flow even when using periodic boundary conditions [55]. A history of computational modeling for wind energy assessment provided by Ayotte [36] highlights the benefits and drawbacks of linear models, RANS models, and LES.

Accurate LES of complex terrain requires turbulent inflow conditions, which is a challenge that has been address in two main ways: synthetic turbulence generation and precursor simulations. Stevens et al. [57] proposed a 'concurrent' method where data is fed directly into main simulation instead of written to disk. They applied this technique to a wind turbine array. A pressure gradient to drive the flow is applied only in the precursor part of the domain. Munters et al. [58] propose a generalization of the precursor method proposed by Stevens et al. [57] that allows for unsteady mean-flow directions. They find that precursor techniques are preferable to synthetic turbulence generation especially for atmospheric boundary layer (ABL) flows. Baba-Ahmadi and Tabor [59] propose and present multiple methods to drive the flow for precursor simulations, based on mapping velocities from a downstream plane of the simulation back to the inlet. They propose to either make corrections to the mapped velocity, such as one to keep the flow rate constant, or introduce a body force to drive the flow while using periodic boundary conditions in the streamwise direction. This latter method was used for a turbulent channel flow precursor simulation by Helgedagsrud et al. [60] with driving pressure gradient and periodic boundary conditions in the streamwise direction to simulate buffeting loads on a bridge section. Tabor and Baba-Ahmadi [61] review treatment of inlet conditions for LES simulations including precursor simulations and synthetic turbulence generation. Lund et al. [62] and Ferrante and Elghobashi [63] used a 'recycling' method where outflow velocity is fed back to the inflow after making adjustments such as keeping the flow rate constant. Li et al. [7] looked at the effect that different inflow conditions have and found that using a pre-simulation of the upstream region gave significantly different results than using an empirical logarithmic law velocity profile.

1.2. Proposed framework for complex-terrain flows

Any LES simulation requires the choice of an appropriate sub-grid scale (SGS) turbulence model and associated constants, to determine parameters such as the eddy viscosity, which only models dissipation associated with turbulent motions. The variational multi-scale (VMS) concept for LES, and its residual-based instantiation called RBVMS [64], do not rely on eddy-viscosity based modeling of turbulence. The main idea of the VMS formulation, proposed by Hughes et al. [65] and refined in Hughes et al. [66] and Bazilevs et al. [64], is to use variational projections in place of the classical filtered equation approach of LES. Avoidance of filters eliminates the difficulties associated with the use of complex filtered quantities. VMS methods avoid filtering through *a priori* separation of scales. Initially, in [66], a turbulent eddy viscosity model was used only in the discretization of the small-scale equations in order to have dissipation acting only on these small scales. By contrast, in a more recent RBVMS formulation [64], the small scales are not explicitly discretized. Instead, the unresolved fine-scales are modeled as functions of the coarse-scale residuals of the Navier–Stokes partial differential equations, and are introduced directly into the coarse-scale equations. An additional challenge of the LES models, including RBVMS, is the mesh resolution requirement near the solid surfaces where the turbulent boundary layers form (i.e., the terrain surface in the present application). This challenge is addressed in [67] by means of the weakly enforced essential (Dirichlet) boundary condition formulation.

Most RANS and LES simulations use finite volume discretization, whereas the VMS framework relies traditionally on the finite element method (FEM). An alternative approach is the concept of isogeometric analysis (IGA), proposed in [68]. It has many similarities to the finite element method, but aims to be geometrically exact by using methods that are common in Computer Aided Design (CAD). The traditional IGA methodology is based on NURBS (Non-Uniform Rational B-Splines), which are commonly used in CAD software and from which a NURBS mesh can be created. NURBS basis functions have several advantages over classical FEM functions. One of the advantages is that NURBS basis functions have $p-1$ continuous derivative across the element boundaries for pth order functions. The higher-order continuity allows to capture the complex flow phenomena more accurately. Once a coarse NURBS mesh is defined, it can be refined through knot insertion without changing the underlying geometry it represents, enabling more accurate h-refinement.

The use of NURBS can eliminate some approximation of the problem domain geometry. Many authors working on atmospheric flow over complex terrains describe a procedure of mesh generation that involves creating a NURBS surface (generally using a CAD software package) to represent the terrain. For example, Makridis [44] describes creating a surface to represent the Askervein hill using the NURBS based 3D modeling software Rhino. Rasouli and Hangan [40] describe a similar process of creating a surface model in a NURBS format. The next step is usually to discretize this NURBS surface into straight-sided finite elements or finite volumes, thus effectively reducing the order of geometry approximation to linear. As an alternative, the fluid domain can also be discretized into volumetric NURBS elements that conform to the original CAD description of the surface, eliminating the need for lower-order approximation of the terrain surface. NURBS have been shown to perform well for wall-bounded turbulent flow simulations. For example, [64] found that quadratic NURBS performed significantly better on coarse meshes (practically matching the first- and second-order statistics from direct numerical simulation) than linear elements for turbulent channel flow. In the present work, we use NURBS to discretize the domain of complex topography, which we believe represents a novel contribution to flow modeling over complex terrains.

The numerical framework based on VMS formulation using both FEM and NURBS discretization has been successfully applied to a wide variety of complex engineering problems, including wind turbines [69–83], aerodynamics of bridge cross-section [84,85], fluid mechanics for stratified flows [81,86–88], hydrokinetic turbines [89–92], bioinspired aerodynamics and FSI [70,71,93–97], flow analysis of turbocharger turbines and other turbomachinery [98–102], flow and thermo-fluid analysis of ground vehicles, tires and brakes [103–108], parachutes [109–111], patient-specific cardiovascular fluid mechanics and FSI [70,71,112–123], biomedical-device FSI [124–127].

The framework used in this paper does not include effect of thermal stratification, although the Boussinesq approximation has been previously developed in the VMS framework in [86]. The remainder of this paper is organized as follows. Section 2 describes the mathematical details of the modeling framework employed. Results

for the Gaussian hill and Bolund hill simulations are presented in Sections 3 and 4, respectively. Conclusions are drawn and future research directions are outlined in Section 5.

2. Modeling framework

2.1. Governing equations

The governing equations are the Navier–Stokes equations of incompressible flows composed of the balance of linear momentum,

$$\rho\left(\frac{\partial \mathbf{u}}{\partial t}+\mathbf{u}\cdot\nabla\mathbf{u}-\mathbf{f}\right)-\nabla\cdot\boldsymbol{\sigma}=\mathbf{0}, \tag{1}$$

and mass,

$$\nabla\cdot\mathbf{u}=0. \tag{2}$$

In the above equations, ρ is the fluid density, $\mathbf{u}$ is the fluid velocity, and $\mathbf{f}$ is the fluid body force per unit mass. The fluid Cauchy stress, $\boldsymbol{\sigma}$, is defined as $-p\mathbf{I}+2\mu\boldsymbol{\varepsilon}(\mathbf{u})$, where p is the pressure, $\mathbf{I}$ is the identity tensor, μ is the dynamic viscosity, and $\boldsymbol{\varepsilon}(\mathbf{u})=\frac{1}{2}(\nabla\mathbf{u}+\nabla\mathbf{u}^T)$ is the strain rate tensor. The essential boundary condition (i.e. the prescribed velocity $\mathbf{g}$) for Eq. (1) is defined on Γ_g part of the domain boundary Γ

$$\mathbf{u}=\mathbf{g}, \tag{3}$$

and natural boundary condition (i.e. the prescribed traction $\mathbf{h}$) is defined on Γ_h part of the domain boundary Γ as

$$\boldsymbol{\sigma}\mathbf{n}=\mathbf{h}, \tag{4}$$

where $\mathbf{n}$ is the unit outward normal vector.

Given the trial function space $\mathcal{S}$, the test function space $\mathcal{V}$, and the problem domain Ω, the weak form of the governing equations may be stated as: Find the velocity–pressure pair $\{\mathbf{u},p\}\in\mathcal{S}$ such that for all test functions $\{\mathbf{w},q\}\in\mathcal{V}$,

$$\int_\Omega \mathbf{w}\cdot\rho\left(\frac{\partial \mathbf{u}}{\partial t}+\mathbf{u}\cdot\nabla\mathbf{u}-\mathbf{f}\right)\mathrm{d}\Omega+\int_\Omega \boldsymbol{\varepsilon}(\mathbf{w}):\boldsymbol{\sigma}(\mathbf{u},p)\mathrm{d}\Omega+\int_\Omega q\nabla\cdot\mathbf{u}\mathrm{d}\Omega=\int_{\Gamma_h}\mathbf{w}\cdot\mathbf{h}\mathrm{d}\Gamma, \tag{5}$$

2.2. The RBVMS framework

Following the VMS methods of [65,66] we additively decompose the solution and test function spaces into coarse and fine-scale sub-spaces. The coarse-scale is resolved by spatial discretization, and the associated spaces and variables are indicated by a superscript h. The fine-scales are those which cannot be represented by the finite spatial discretization, and the associated spaces and variables are indicated with a prime symbol ($'$).

Following the RBVMS approach in [64], we decompose the solution variables as $\mathbf{u}=\mathbf{u}^h+\mathbf{u}'$ and $p=p^h+p'$, choose for the test functions to be $\mathbf{w}=\mathbf{w}^h$ and $q=q^h$ to generate the coarse-scale equations, and model the unresolved fine-scales as

$$\mathbf{u}'=-\frac{\tau_{\mathrm{SUPS}}}{\rho}\mathbf{r}_{\mathrm{M}}(\mathbf{u}^h,p^h), \tag{6}$$

$$p'=-\rho\nu_{\mathrm{LSIC}}r_{\mathrm{C}}(\mathbf{u}^h), \tag{7}$$

where the coarse-scale residuals of the momentum and continuity differential equations are given by

$$\mathbf{r}_{\mathrm{M}}(\mathbf{u}^h,p^h)=\rho\left(\frac{\partial \mathbf{u}^h}{\partial t}+\mathbf{u}^h\cdot\nabla\mathbf{u}^h-\mathbf{f}^h\right)-\nabla\cdot\boldsymbol{\sigma}(\mathbf{u}^h,p^h),\quad\text{and} \tag{8}$$

$$r_{\mathrm{C}}(\mathbf{u}^h)=\nabla\cdot\mathbf{u}^h. \tag{9}$$

The above residual-based models for the fine-scales are inferred from the fine-scale equations, which are obtained by setting $\mathbf{w}=\mathbf{w}'$ and $q=q'$. (See [64] for more details.)

Substituting the above expressions into Eq. (5), the resulting RBVMS formulation may be stated as follows: find $\{\mathbf{u}^h, p^h\} \in \mathcal{S}^h$, such that $\forall \{\mathbf{w}^h, q^h\} \in \mathcal{V}^h$

$$\begin{aligned}
&\int_\Omega \mathbf{w}^h \cdot \rho \left(\frac{\partial \mathbf{u}^h}{\partial t} + \mathbf{u}^h \cdot \nabla \mathbf{u}^h - \mathbf{f}^h \right) \mathrm{d}\Omega + \int_\Omega \boldsymbol{\varepsilon}\left(\mathbf{w}^h\right) : \boldsymbol{\sigma}\left(\mathbf{u}^h, p^h\right) \mathrm{d}\Omega + \int_\Omega q^h \nabla \cdot \mathbf{u}^h \mathrm{d}\Omega - \int_{\Gamma_h} \mathbf{w}^h \cdot \mathbf{h} \mathrm{d}\Gamma \\
&+ \sum_{e=1}^{n_{el}} \int_{\Omega^e} \tau_{\mathrm{SUPS}} \left(\mathbf{u}^h \cdot \nabla \mathbf{w}^h + \frac{\nabla q^h}{\rho} \right) \cdot \mathbf{r}_{\mathrm{M}}\left(\mathbf{u}^h, p^h\right) \mathrm{d}\Omega \\
&+ \sum_{e=1}^{n_{el}} \int_{\Omega^e} \rho \nu_{\mathrm{LSIC}} \nabla \cdot \mathbf{w}^h \mathrm{r}_{\mathrm{C}}\left(\mathbf{u}^h\right) \mathrm{d}\Omega \\
&- \sum_{e=1}^{n_{el}} \int_{\Omega^e} \tau_{\mathrm{SUPS}} \mathbf{w}^h \cdot \left(\mathbf{r}_{\mathrm{M}}\left(\mathbf{u}^h, p^h\right) \cdot \nabla \mathbf{u}^h \right) \mathrm{d}\Omega \\
&- \sum_{e=1}^{n_{el}} \int_{\Omega^e} \frac{\nabla \mathbf{w}^h}{\rho} : \left(\tau_{\mathrm{SUPS}} \mathbf{r}_{\mathrm{M}}\left(\mathbf{u}^h, p^h\right) \right) \otimes \left(\tau_{\mathrm{SUPS}} \mathbf{r}_{\mathrm{M}}\left(\mathbf{u}^h, p^h\right) \right) \mathrm{d}\Omega = \mathbf{0}.
\end{aligned} \tag{10}$$

Here, Ω is divided into n_{el} elements denoted by Ω^e. The stabilization parameters in Eq. (10) are given by

$$\tau_{\mathrm{SUPS}} = \left(\frac{4}{\Delta t^2} + \mathbf{u}^h \cdot \mathbf{G}\mathbf{u}^h + C_I \nu^2 \mathbf{G} : \mathbf{G} \right)^{-1/2}, \tag{11}$$

and

$$\nu_{\mathrm{LSIC}} = \left(\mathrm{tr}\mathbf{G}\tau_{\mathrm{SUPS}}\right)^{-1}, \tag{12}$$

where tr$\mathbf{G}$ is the trace of the element metric tensor $\mathbf{G}$ given by

$$\mathbf{G} = \left(\frac{\partial \boldsymbol{\xi}}{\partial \boldsymbol{x}} \right)^T \frac{\partial \boldsymbol{\xi}}{\partial \boldsymbol{x}}, \tag{13}$$

$\boldsymbol{\xi}$ and $\boldsymbol{x}$ are the element parametric and physical coordinates, respectively, Δt is the time-step size, and C_I is the constant of the element-wise inverse estimate [128]. For the simulations with linear FEM and with quadratic NURBS $C_I = 3$. For more details on the stabilization parameters, including some of the newer ones, see [96,129–133].

2.3. Weakly enforced no-slip boundary conditions

Weakly enforced no-slip essential (Dirichlet) boundary conditions are implemented on the terrain surface. The method, introduced in [67] was shown to relax the grid resolution requirements near the wall while preserving the overall solution accuracy. In the weak boundary-condition methodology, rather than requiring the solution to exactly satisfy the Dirichlet boundary conditions ("strong satisfaction"), terms are added to the left-hand side of the VMS formulation (Eq. (10)) to enforce the Dirichlet boundary conditions weakly as Euler–Lagrange conditions. These additional terms for a prescribed velocity $\mathbf{g}$ on the Γ_g are:

$$\begin{aligned}
&- \sum_{b=1}^{n_{eb}} \int_{\Gamma^b \cap \Gamma_g} \mathbf{w}^h \cdot \boldsymbol{\sigma}(\mathbf{u}^h, p^h)\mathbf{n} \mathrm{d}\Gamma \\
&- \sum_{b=1}^{n_{eb}} \int_{\Gamma^b \cap \Gamma_g} \left(2\mu \boldsymbol{\varepsilon}(\mathbf{w}^h)\mathbf{n} + q^h \mathbf{n} \right) \cdot \left(\mathbf{u}^h - \mathbf{g} \right) \mathrm{d}\Gamma \\
&- \sum_{b=1}^{n_{eb}} \int_{\Gamma^b \cap \Gamma_g^-} \mathbf{w}^h \cdot \rho \left(\mathbf{u}^h \cdot \mathbf{n} \right) \left(\mathbf{u}^h - \mathbf{g} \right) \mathrm{d}\Gamma \\
&+ \sum_{b=1}^{n_{eb}} \int_{\Gamma^b \cap \Gamma_g} \tau_{\mathrm{B}} \mathbf{w}^h \left(\mathbf{u}^h - \mathbf{g} \right) \mathrm{d}\Gamma.
\end{aligned} \tag{14}$$

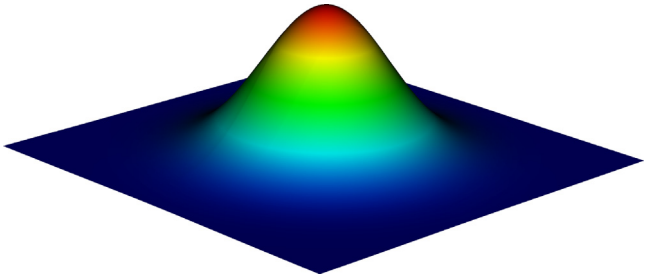

Fig. 1. Isometric view of the Gaussian hill. The vertical coordinate is scaled by a factor of five for visibility, and the image is cropped in the horizontal direction with respect to the simulation domain.

Here, $\Gamma_g^- = \left\{\mathbf{x} | \mathbf{u}^h \cdot \mathbf{n} < 0, \forall \mathbf{x} \in \Gamma_g\right\}$ is the inflow part of Γ_g, and τ_{B} is the stabilization parameter given by

$$\tau_{\mathrm{B}} = \frac{C_I^B \mu}{h_n}, \tag{15}$$

where C_I^B is a positive constant computed from an appropriate element-level inverse estimate (for linear FEM and quadratic NURBS we used $C_I^B = 4$), and h_n is the wall-normal element size that can be computed as

$$h_n = (\mathbf{n} \cdot \mathbf{G}\mathbf{n})^{1/2}. \tag{16}$$

2.4. Discretization methods

In the present work, comparison is made between linear FEM and quadratic NURBS [68] to discretize Eq. (10) for the Gaussian Hill example. The second-order accurate, implicit, generalized-α time integration scheme is employed for time discretization. At each time step, the resulting non-linear system of equations is solved using Newton–Raphson algorithms. At every non-linear iteration, the linear system of equations is solved using generalized minimum residual (GMRES) method.

3. Axisymmetric Gaussian hill

We simulate 3D, axisymmetric Gaussian hill (normally distributed surface) given by $z = h \cdot \exp\left(-0.5(r/\sigma)^2\right)$ where r and z are radial and vertical coordinates, respectively, $h = 700\,\mathrm{m}$ is the height of the hill, and $\sigma = L/1.1774$. $L = 1750\,\mathrm{m}$ is the hill length defined as the value of r where $z = h/2$. Values for L and h, are taken from Prospathopoulos and Politis [43] who simulate the same cases tested here using a RANS solver CRES-flow NS, with $k - \omega$ turbulence model. Our computational domain spans 23 km in the streamwise direction and spanwise directions. These dimensions are found necessary to ensure independence of the solution from boundary effects. The domain height is 5000 m. An isometric view of the Gaussian hill is shown in Fig. 1.

A logarithmic velocity profile,

$$U = U_{ref} \frac{u_*}{\kappa} \ln \frac{z}{z_0}, \tag{17}$$

is applied at the inlet, where $\kappa = 0.41$ is von-Karmann constant, $z_0 = 2.29 \times 10^{-7}\,\mathrm{m}$ is the roughness length, and $u_* = \frac{\kappa}{\ln \delta/z_0}$ is the friction velocity, where $\delta = 500\,\mathrm{m}$ is the chosen atmospheric boundary layer thickness. The reference velocity $U_{ref} = 10.9\,\mathrm{ms}^{-1}$ is chosen such that the velocity at 90 m elevation $U_{90} = 10\,\mathrm{ms}^{-1}$. No-slip boundary condition is enforced on the terrain surface. Grid convergence analysis is performed using the strongly enforced no-slip boundary condition which is followed by comparison to the weakly enforced no-slip boundary condition. No fluid penetration is allowed on the sides and the top of the domain. The outflow boundary uses the naturally imposed traction-free condition.

Table 1
Mesh resolution and GCI (FEM)

	Elements	Refinement ratio	Velocity [m/s]	GCI (%)
Coarse	108 × 102 × 25	–	8.43	–
Medium	120 × 132 × 50	1.42	8.51	3.2
Fine	144 × 192 × 100	1.52	8.65	4.5

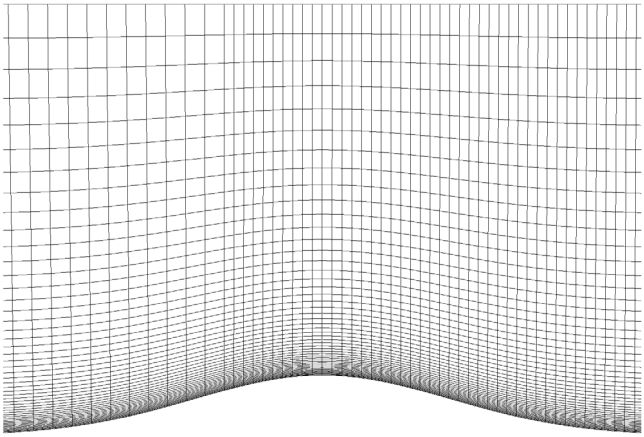

Fig. 2. Cross-section of the domain with hexahedral mesh along centerline of Gaussian hill.

3.1. Gaussian hill with linear FEM

The computational domain is discretized into structured, hexahedral elements. The time step of $dt = 1.0\,\mathrm{s}$ is used for 11×10^3 s before flow quantities are averaged for another 6×10^3 s, corresponding to approximately 63 and 32 advection hill lengths, respectively. This gives the statistically stationary flow behavior. Three different mesh resolutions are used, referred to as coarse, medium, and fine. The same time step size is used for all mesh resolutions. The number of elements used in the streamwise, spanwise, and wall normal directions is shown in Table 1. The minimum CFL number varies from 0.3 for the coarse mesh to 0.8 for the fine mesh. Table 1 also shows the grid convergence index (GCI) based on Richardson extrapolation [134] which is computed for the minimum time averaged streamwise velocity downstream of the hill at 90 m elevation and is less than 5% for coarse to medium and medium to fine meshes. In the streamwise and spanwise directions the grid is uniformly spaced with the exception of a refinement region between $x \in [-1140, 5700]$ in the streamwise direction and $y \in [-684, 684]$ in the spanwise direction. In the vertical direction the grid spacing increases with elevation from 6 m at the terrain surface to 342 m at the upper far field boundary, following hyperbolic tangent distribution. The vertical coordinate of the kth grid point is given by $z_k = 5000 \cdot (\tanh(2.5 \cdot (z_{uk} - 1))/\tanh(2.5) + 1)$, where z_{uk} is the vertical coordinate for a uniform grid spacing, and 5000 is the domain height. A cross-section of the computational domain down the centerline along the streamwise direction for the medium mesh is shown in Fig. 2.

Time averaged streamwise velocity 90 m above the terrain surface, for the three different mesh resolutions, is plotted along the length of the domain (x) in Fig. 3. All three mesh resolutions show similar maximum velocity over the top of the hill at $x = 0$, with a value about 2% larger than that predicted by [43] (note the non-zero origin on the vertical axis). A slight discrepancy is seen at around the location of the minimum velocity on the downstream side of the hill with the current simulation predicting slightly more slowdown in streamwise velocity.

3.2. Gaussian hill with quadratic NURBS

We next simulate the Gaussian hill using IGA based on NURBS. A NURBS surface is constructed to represent the surface of the Gaussian hill using CAD software. This surface is used as a ‘coarse’ mesh, and successive refinement is performed without altering the geometry by knot insertion. This process is actually a simplification

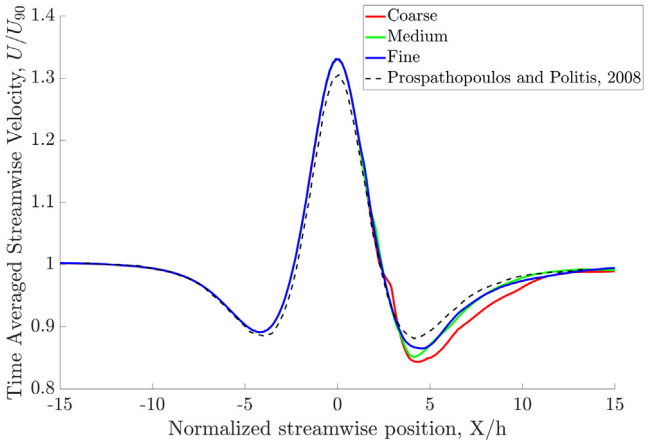

Fig. 3. Normalized time averaged streamwise velocity 90 m above Gaussian hill for three grid resolutions with linear FEM.

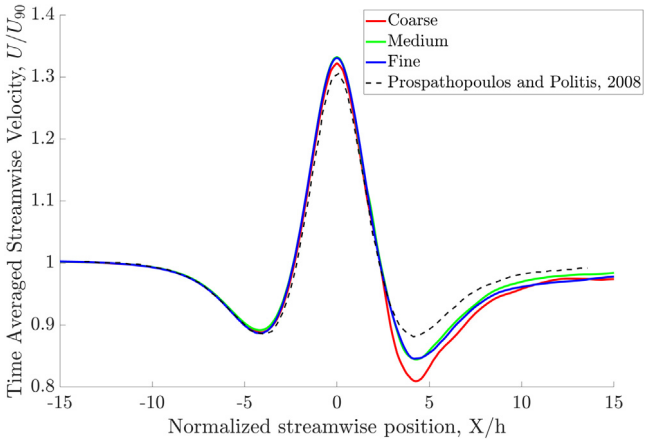

Fig. 4. Normalized time averaged streamwise velocity 90 m above Gaussian hill for three grid resolutions with quadratic NURBS.

from the linear finite element approach of the previous section, as for that process the Gaussian hill is initially constructed as a NURBS surface, which is then approximated by bi-linear quadrilateral surface elements during meshing. The same boundary conditions and time-step as described above for the FEM case are used. The number of NURBS elements, defined as knot spans as in [68], is chosen to be the same as for the finite element meshes.

Time averaged streamwise velocity 90 m above the terrain surface is plotted in Fig. 4 for simulations using quadratic NURBS. The maximum velocity predicted by the NURBS simulation for the fine resolution is again about 2% higher than the data from [43]. The minimum velocity on the downstream side of the hill is about 4% lower for the fine resolution than the published data. The medium and fine resolutions agree very closely over this region indicating the medium resolution would likely be sufficiently fine in this case. Fig. 5 shows an isometric view of the Gaussian surface along with the U component of velocity down the center of the domain.

The GCI for the minimum velocity behind the hill at 90 m elevation is 0.14% for the coarse to medium mesh and 0.002% for the medium to fine mesh, which, as expected due to the higher order of the shape functions, is much better than the GCI for the linear FEM case.

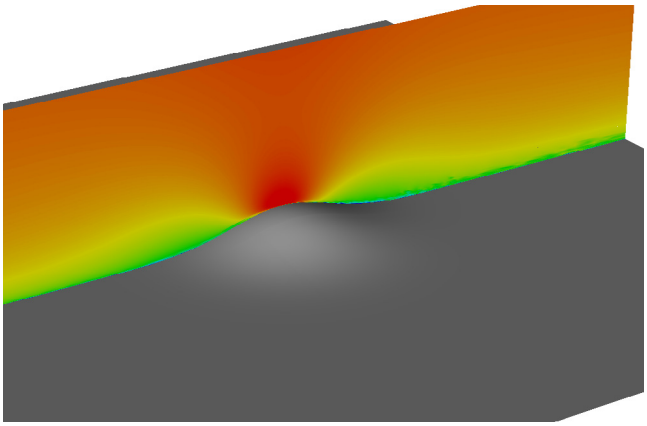

Fig. 5. Time averaged streamwise velocity component for the fine mesh resolution Gaussian hill using NURBS.

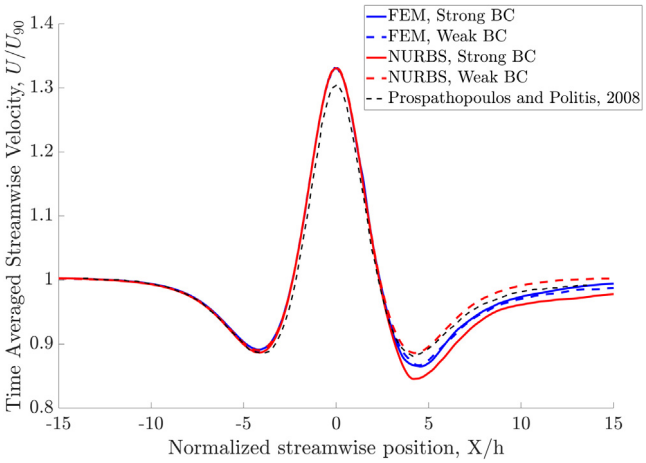

Fig. 6. Gaussian hill streamwise velocity using strong and weak enforcement of the Dirichlet (no-slip) boundary condition. All simulations are for the fine mesh resolution.

3.3. Gaussian hill with weakly enforced no-slip boundary condition on the terrain surface

The benefit of employing the weakly-enforced no-slip boundary condition on the terrain surface, as presented in Section 2.3 is investigated next. We compare the usual no-slip boundary condition (strongly enforced) to the weakly-enforced boundary condition for the fine mesh using both linear FEM and quadratic NURBS. The comparison of streamwise velocity 90 m above the terrain surface is shown in Fig. 6 for the fine-resolution FEM and NURBS simulations. The simulation using weak enforcement of the no-slip condition shows less slowdown after the hill, more closely matching the published data from [43]. The combination of relaxing the no-slip condition and using higher-order accurate and smooth NURBS basis functions allows the simulation to more accurately capture the flow profile in the recirculation region. On the other hand, very little improvement can be observed for the FEM simulations. This can be due to the selection of the stabilization parameters, and specifically the inverse-estimate constant. We will investigate this in more detail in the further studies.

Comparison of the FEM results to the NURBS results is shown in Fig. 7, where we compare the medium and fine resolutions using the weakly-enforced boundary condition. The downstream side of the hill again highlights differences in the discretization methods used. The largest slowdown is seen with the medium resolution linear FEM simulation. The fine FEM and medium NURBS simulations show fairly similar results, highlighting the increased

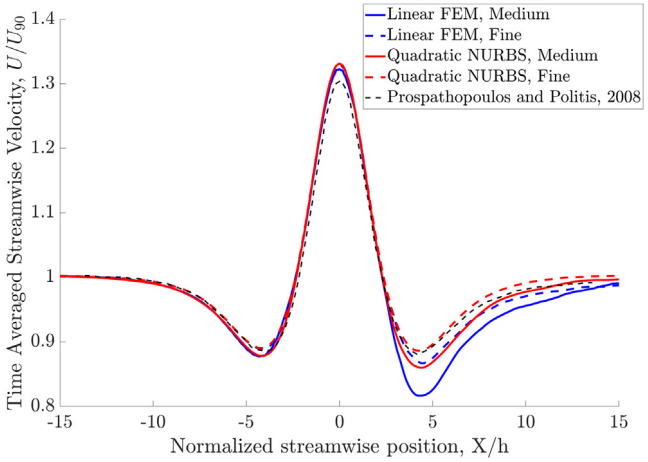

Fig. 7. Normalized streamwise velocity 90 m above the Gaussian hill for linear FEM and quadratic NURBS.

Fig. 8. Bolund hill. *Source:* Picture from Bechmann et al. [39].

resolution necessary for FEM given the lower-order accuracy. The fine resolution NURBS simulation shows results very similar to the published data with the higher order and smooth basis functions better able to capture the sharp velocity gradients in this region.

4. Bolund hill

The Bolund hill (Fig. 8) is a coastal geographical feature in Denmark that was the subject of a field experiment and a "blind" modeling study. The Bolund field campaign provides a new dataset for validation of LES codes for wind energy applications. Bolund hill is considered a difficult modeling problem due to the nearly vertical escarpment on the upwind side of the hill, which produces complex 3D flow. Data was collected and used to validate models predicting flow in complex terrains [25,26].

The hill is approximately 12 m high, 130 m long and 75 m wide, and is surrounded by water on three sides. The remaining side (on the downstream end for the case considered here) comprises relatively flat terrain. The incoming flow travels over the ocean, making the inflow boundary condition well defined. Measurements are taken at various heights for each of the 10 mast locations over 10 min periods, with one mast located far upstream of the hill to quantify the free stream velocity profile and turbulent kinetic energy to provide inflow boundary conditions for the simulations. The mast locations are shown in Fig. 9. Additionally, limited effects from stratification are expected due to the small hill height relative to the boundary layer depth, therefore the approximation of neutral stratification employed in the present work is be considered valid.

The domain constructed around Bolund hill stretches 390 m across, 800 m long (300 m upstream and downstream of the hill) and 120 m high. This domain size was recommended by [39].

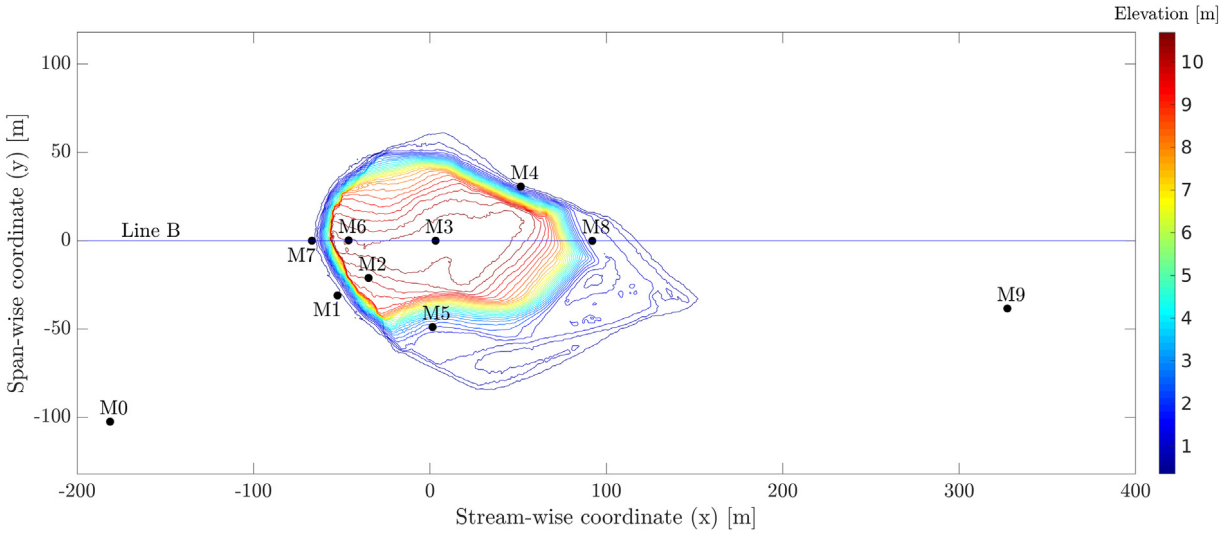

Fig. 9. Bolund hill elevation contours and mast locations. Flow is from left to right in the case considered.

4.1. Precursor simulation

To generate realistic, turbulent inflow conditions for the Bolund hill simulation, a pressure driven NURBS precursor simulation of turbulent flow over a flat plate is used, and sequential planes of the velocity solution are fed into the main simulation. The method is the same as that described in [60] except that we use a half-channel since the no-slip boundary is only on the lower surface of the domain.

Periodic boundary conditions are used in the streamwise and spanwise directions and the no-slip condition is weakly enforced on the lower boundary. Symmetry condition is employed at the upper boundary. The precursor simulation uses a rectangular domain with spanwise and vertical dimensions equal to those of the main simulation domain (390 m and 120 m respectively). In the streamwise direction, the domain extends 750 m. 192, 64, and 32 elements are used in the streamwise, spanwise, and wall-normal directions respectively. The initial condition is a semi-parabolic mean velocity profile based on the bulk velocity with superposed random velocity fluctuations to promote transition to turbulent flow. The flow is driven by a volumetric forcing, f, equal to $3.73 \times 10^{-3}\,\mathrm{ms}^{-2}$. The forcing is calculated based on a desired friction velocity Reynolds number, $Re_\tau = u^* D/\nu = 395$, and bulk velocity, $\overline{U}_b = 11.893\,\mathrm{ms}^{-1}$. The bulk velocity is the mean velocity based on the suggested logarithmic inflow velocity profile [39],

$$u = \frac{u_0^*}{\kappa} \ln\left(\frac{z_{agl}}{z_0}\right), \tag{18}$$

where (z_{agl}) is the height above the ground, $u_0^* = 0.4\,\mathrm{ms}^{-1}$ is the reference friction velocity measured during the experiment (not to be confused with that used for the precursor simulation), $z_0 = 3 \times 10^{-4}\,\mathrm{m}$ is the surface roughness length, and $\kappa = 0.4$ is the von Karman constant.

The friction velocity and surface roughness are set for four different cases in [39] based on fits to experimental data from the upstream mast. The values given refer to Case 1 of [39] with 270° flow direction which is the case simulated in this work. The friction velocity Reynolds number is chosen for two reasons. First, similar simulations and experiments performed at this Reynolds number provide data for validation [60,135]. Secondly, these researchers reported turbulence intensities (TI) of approximately 4.4% for this Re_τ, which is similar to the turbulence level recommended by Bechmann et al. [39], who recommended modelers specify a turbulence kinetic energy value of $TKE = 5.8(u_0^*)^2 = 0.928\,\mathrm{m}^2/\mathrm{s}^2$, constant with elevation. Since both measures of turbulence are based on RMS fluctuations of the diagonal terms of the Reynolds stress tensor, the relation,

$$TI = \frac{\sqrt{\frac{2}{3}TKE}}{\overline{U}_b} = 6.6\%, \tag{19}$$

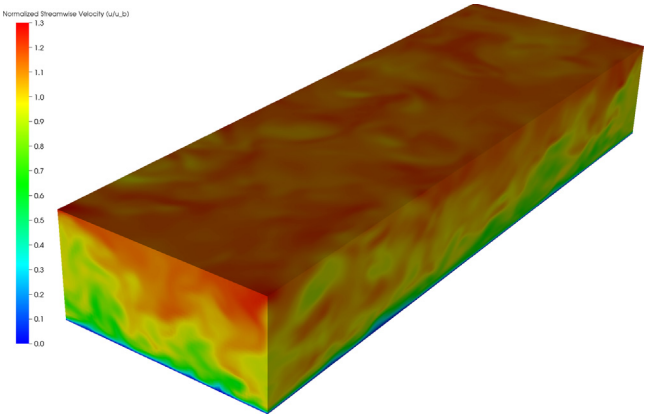

Fig. 10. Instantaneous streamwise velocity normalized by the bulk velocity for the precursor simulation.

can be used. With Re_τ and $\overline{U}_b$ determined, the volumetric forcing f can be found by balancing the volumetric forcing with the wall shear force, giving the expression:

$$f = \frac{u^{*2}}{D}, \tag{20}$$

where D is the domain (half-channel) height, and the friction velocity u^* is found through the equation system formed by Spalding's parameterization for the law of the wall [136], Dean's correlation relating the bulk and center line ($\overline{U}_{cl}$) velocities [137], and the definition of Re_τ. The equations

$$\overline{U}_{cl} = u^* g^{-1}(Re_\tau), \tag{21}$$

$$\overline{U}_{cl} = 1.28\overline{U}_b \left(\frac{2\overline{U}_b D}{\nu}\right)^{-0.0116} = 1.28\overline{U}_b Re_b^{-0.0116}, \tag{22}$$

$$\nu = \frac{u^* D}{Re_\tau}, \tag{23}$$

are solved for $\overline{U}_{cl}, u^*$, and ν simultaneously as described in [60]. Other quantities, namely, $Re_\tau, \overline{U}_b$ and D are known, and g^{-1} is the inverse of Spalding's parameterization of the law-of-the wall,

$$g(u^+) = u^+ + e^{-\chi B}\left(e^{\chi u^+} - 1 - \chi u^+ - \frac{(\chi u^+)^2}{2!} - \frac{(\chi u^+)^3}{3!}\right), \tag{24}$$

where $\chi = 0.4$ and $B = 5.5$.

The simulation is run for 17,000 steps with a time step $\Delta t = 0.2$ s, corresponding to the flow traveling over 50 times the domain length. The mean velocity profile was seen to converge to the Direct Numerical Simulation (DNS) results prior to this point. Fig. 10 shows instantaneous streamwise velocity contours for the precursor simulation.

Time averaged velocity and velocity fluctuation profiles are presented in terms of non-dimensional wall distance (y^+) and velocity (u^+) units given by

$$y^+ = \frac{yu^*}{\nu} = \frac{yRe_\tau}{D}, \tag{25}$$

$$u^+ = \frac{u}{u^*} = \frac{uD}{Re_\tau \nu}. \tag{26}$$

The profiles are shown in Figs. 11 and 12 and the results are very close to the DNS data from Moser et al. [135].

Comparing the results of the pressure driven, periodic, half-channel precursor simulation with the inflow boundary conditions suggested by Bechmann et al. [39] (Fig. 13), there is slight deviation in the mean velocity profile from the log-law profile recommended, but generally good overall agreement is achieved. The recommendation of setting turbulence kinetic energy to a constant value with elevation is not physical, as evidenced by the precursor simulation (Fig. 14). However, the values are in a similar range.

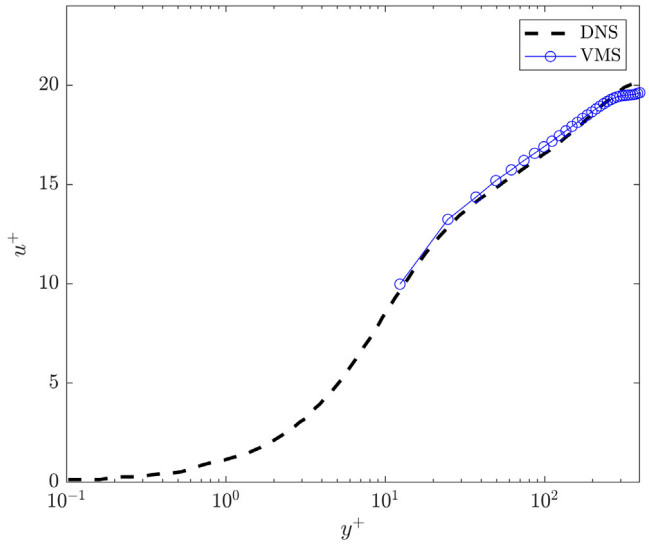

Fig. 11. Mean streamwise velocity of the precursor simulation vs. distance from the wall in non-dimensional units. DNS data from Moser et al. [135].

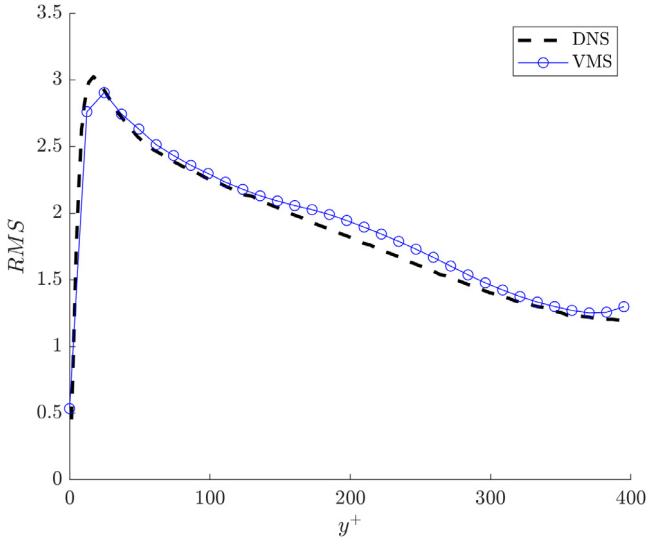

Fig. 12. Root mean square (RMS) of the streamwise velocity fluctuations of the precursor simulation versus distance from the wall in non-dimensional units. DNS data from Moser et al. [135].

4.2. Bolund hill precursor coupling

Data transfer from the precursor simulation to the inflow of the Bolund hill simulation is done using the method described in [60] and is based on weakly enforced boundary conditions. After the simulation reached a statistically stationary state as described in the results section above, successive (in time) planes of the inflow/outflow precursor boundary are fed into the main Bolund hill simulation. As the precursor and Bolund hill mesh do not match one-to-one at the inlet plane, a coupling method is needed to transfer the data. The velocities from the precursor simulation are output (written to disk) at the locations of the integration points of the main simulation. These values are read by the main simulation and enforced weakly on the inflow boundary by setting them equal to the inflow boundary velocity **g** from Eq. (14).

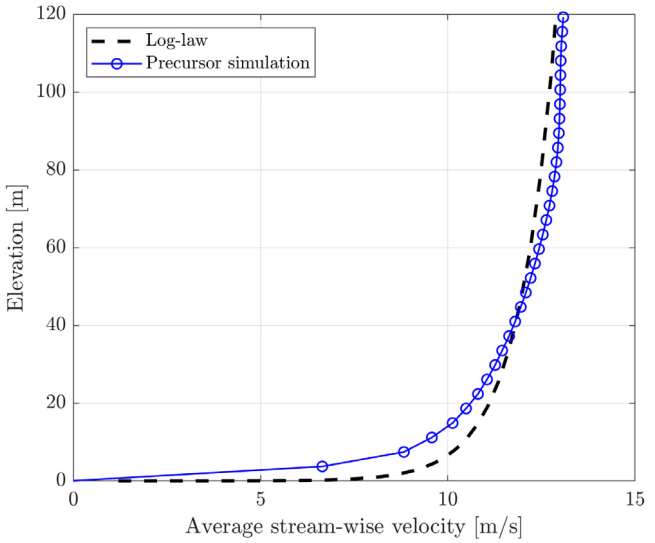

Fig. 13. Time averaged streamwise velocity profile compared with the log-law profile proposed at inlet condition by Bechmann et al. [39].

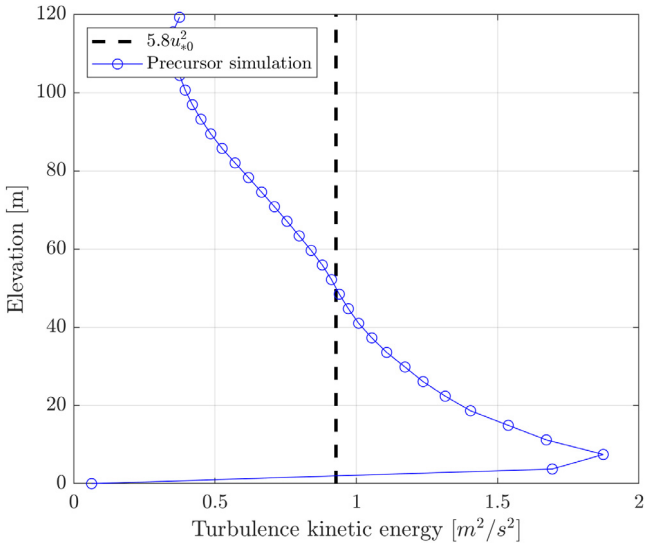

Fig. 14. Turbulent kinetic energy profile compared with the constant value proposed as inlet condition by Bechmann et al. [39].

4.3. Bolund hill main simulation with quadratic NURBS

The Bolund hill domain is discretized using quadratic NURBS elements. We decided to forego the FEM discretization for this problem due to the superior performance of NURBS-based simulations for the Gaussian hill presented earlier in the paper. The NURBS mesh is comprised of 275 $\times$ 161 $\times$ 57 elements (2.52 million in total) in the streamwise, spanwise, and vertical directions, respectively. The first element in the vertical direction is located at 0.5 m. To capture the sharp terrain gradient on the upwind side of the hill, the mesh is refined in the streamwise direction over a distance of 18 m. A cross section of the mesh is shown in Fig. 15.

The inlet condition at each time step is taken from the precursor simulation, which is run with the same time step as the main simulation. The precursor simulation has the same spanwise and vertical dimensions as the main simulation but a different mesh resolution. The minimum CFL number for this set-up is 0.8. On the side boundaries,

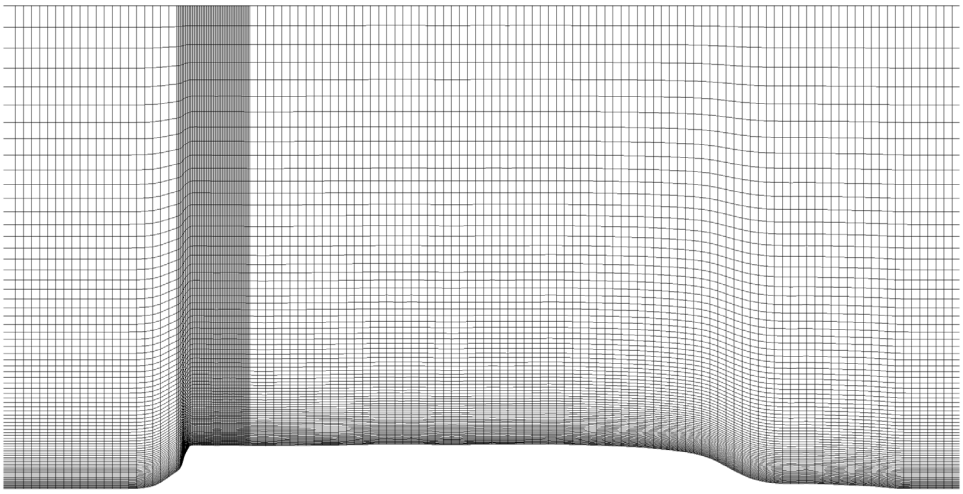

Fig. 15. Cross-section of the mesh for the Bolund hill simulation.

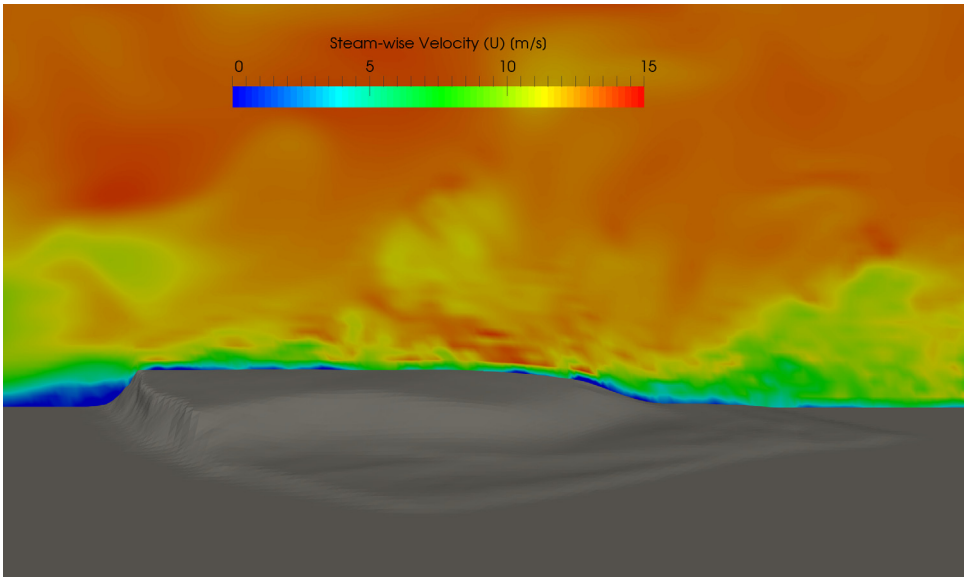

Fig. 16. Instantaneous streamwise velocity contours on the $y = 0$ plane.

no-penetration and zero tangential traction boundary conditions are imposed. The outlet is assumed to be traction-free, with the backflow stabilization terms added to preclude divergence in the computations due to possible local flow recirculation at the outlet [138]. On the terrain surface, the no-slip boundary condition is enforced weakly. The initial condition is set based on a logarithmic velocity profile with elevation over the entire domain, as per Eq. (18).

Fig. 16 shows instantaneous streamwise velocity contours along the $y = 0$ plane, Fig. 17 shows the time averaged streamwise velocity on the same plane, and Fig. 18 shows the time averaged velocity streamlines over the upwind slope of the hill, where a re-circulation region is seen just behind the edge of the upwind slope.

Simulation results are compared to field measurements at each mast location shown in Fig. 9. Vertical profiles of the flow speed S are shown in Figs. 19 and 20. The results are non-dimensionalized by the reference friction velocity $u_0^* = 0.4\,\mathrm{ms}^{-1}$ from Eq. (18). The simulation results match the measure data quite well in most locations.

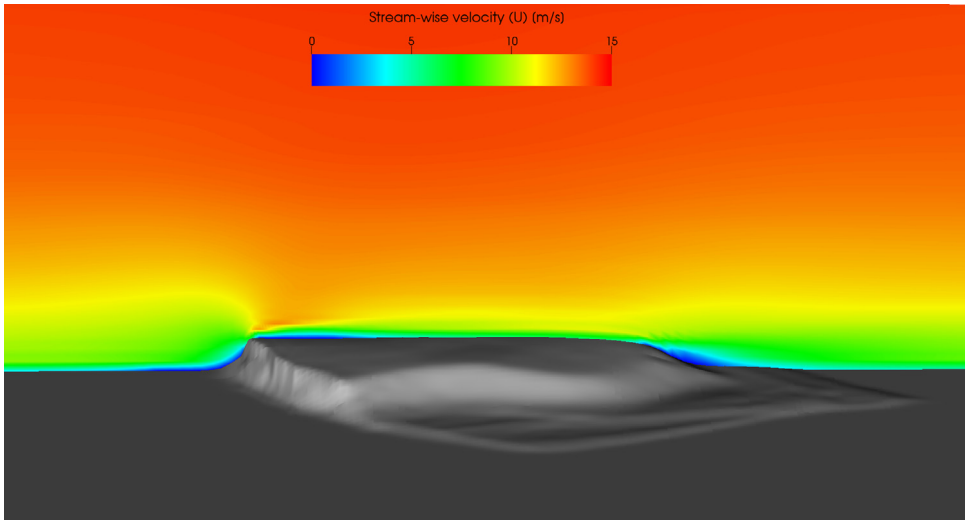

Fig. 17. Time averaged streamwise velocity contours on the $y = 0$ plane.

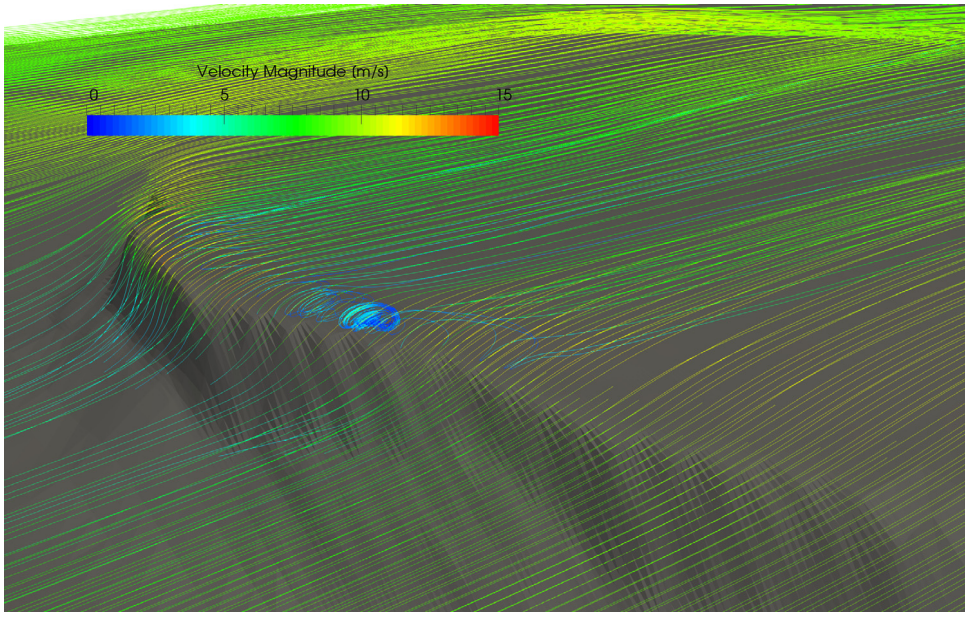

Fig. 18. Time averaged velocity streamlines colored by flow speed. (For interpretation of the references to color in this figure legend, the reader is referred to the web version of this article.)

The location of specific masts can provide insight into the aspects of the flow that are best captured by the simulation. Masts 1 and 7 are located just in front of the hill. Masts 2 and 6 are located at the top of hill just behind the steep slope on the upstream side. Masts 4, 5, and 8 are located at the base of the hill on the downstream side, and mast 3 is located in the middle of the broad, nearly flat expanse on the top of the hill. The simulations show very good match to the experimental data at masts 1 and 7, i.e. correctly capturing the velocity slowdown in front of the hill. Mast 2 and mast 5, located in recirculated regions just after the upstream slope and just after the downstream slope respectively, show slight over-prediction of the velocity close to the surface (below 5 m elevation). The simulations also show good agreement with the experimental measurements near the ground where the velocity gradients are high and agreement with the experimental data is hard to achieve.

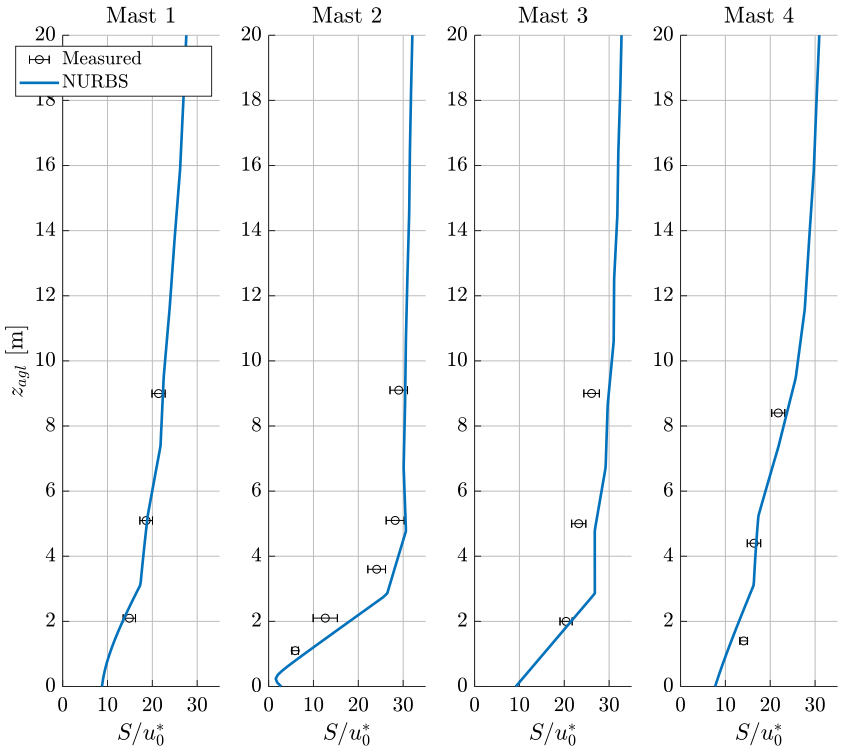

Fig. 19. Mean velocity magnitude profiles comparing NURBS simulations with measured data.

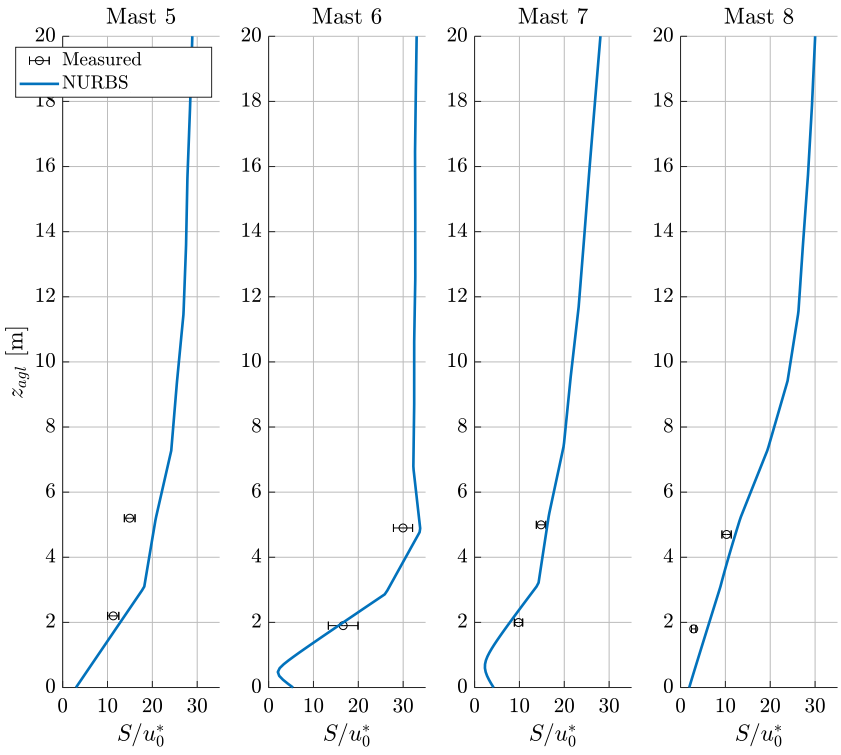

Fig. 20. Mean velocity magnitude profiles comparing NURBS simulations with measured data.

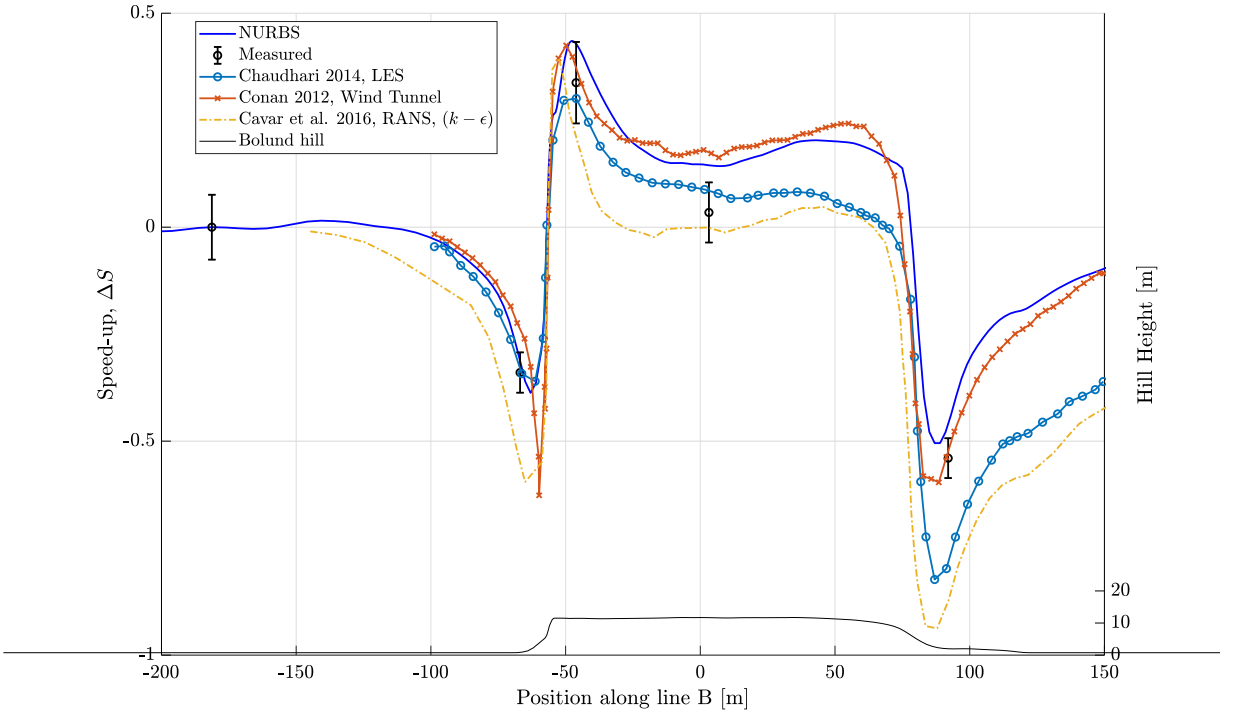

Fig. 21. Velocity speed-up 5 m above ground level along line B.

Comparison of the simulation results with measurements for the Bolund hill case is often presented in terms of the relative velocity difference from an upstream reference location. Fig. 21 plots the velocity speed-up along a horizontal line 5 m above the ground along the transect 'line B' (see Fig. 9). The velocity speed-up is defined as

$$\Delta S = \frac{\overline{s}_{z_{agl}} - \overline{s_0}_{z_{agl}}}{\overline{s_0}_{z_{agl}}} \tag{27}$$

where the over-bar indicates a time average and the reference velocity magnitude, s_0, is calculated 5 m above the ground at the location of Mast 0 (Fig. 9) in the inflow region of the domain. The measured data points are shown with open circle markers and the terrain profile is plotted near the bottom of the figure with the elevation corresponding to the vertical axis on the right-hand side. The simulations accurately predict the velocity slowdown just in front of the hill, and are also within one standard deviation of the measured value at the tower just after the top of the hill. The simulations, however, slightly over-predict the velocity magnitude in the middle of the broad flat area on top of the hill. The velocity slowdown on the lee side of the hill is well captured. The results of previously published studies on Bolund hill are also plotted in Fig. 21, including LES from Chaudhari [46], a wind tunnel experiment by Conan et al. [4], and RANS simulation from [48]. The NURBS simulation shows favorable comparison to the measured data and wind tunnel data, and follow the trend very well when compared to other numerical studies.

5. Conclusions

Accurate prediction of local flow field in complex terrain is critical for many engineering applications, including wind energy, which requires the development of a high-fidelity framework to better model the atmospheric flows over complex geographical terrains. In this paper we applied an RBVMS framework in conjunction with FEM and NURBS-based discretization to simulate representative areas of complex terrain. The model was validated using two well documented cases of airflow over complex terrain, the Gaussian hill (normally distributed surface) and Bolund hill (the actual geographical terrain). We found that the RBVMS formulation showed excellent agreement with published data for both cases. The simulations with quadratic NURBS discretization showed better accuracy for the Gaussian hill than linear FEM due to the higher-order continuity of the NURBS basis functions. Moreover,

we also highlighted the need for special treatment of the no-slip boundary condition at the terrain surface. The weakly-enforced formulation of the no-slip boundary condition was used for both NURBS and FEM discretization. Going from strong to weak imposition of the boundary condition significantly improves the result for NURBS-based simulation, but very little improvement was observed for the FEM simulations. This can be due to the selection of the stabilization parameters, and specifically the inverse-estimate constant. We will investigate the sensitivity of the results to the selection of these parameters in the further studies. Simulations using a quadratic NURBS discretization was also performed for the Bolund hill showing favorable comparison with the measurements and wind tunnel experiments, and following the trend very well with the numerical results reported by others. These results indicate great potential of the proposed framework to predict airflow over complex terrains.

Future work will continue to examine cases of highly complex terrains such as the Perdigão location. The Perdigão location was recently the subject of a large-scale field study, as part of the New European Wind Atlas, to investigate flow in complex terrains, including the interaction of wind turbine wakes with the terrain. We also plan to perform numerical simulations using NURBS discretization for atmospheric boundary layer flow with different stratification regimes, which has a significant impact on the flow behavior over the terrain, and especially when interacting with wind turbines. Finally, we plan to perform simulations of the entire wind farm under realistic stratified turbulent flow conditions in a complex terrain.

Declaration of competing interest

The authors declare that they have no known competing financial interests or personal relationships that could have appeared to influence the work reported in this paper.

Acknowledgments

M. Ravensbergen and A. Korobenko was partially supported by NSERC, Canada Discovery Grant, RGPIN-2017-03781. Y. Bazilevs was supported through the National Science Foundation (NSF), USA Award No. 1854436. We thank Compute Canada and Advanced Research Computing (ARC) at the University of Calgary for providing HPC resources that have contributed to the research results reported in this paper.

References

[1] J.C. Barnard, An evaluation of three models designed for siting wind turbines in areas of complex terrain, Sol. Energy 46 (5) (1991) 283–294, http://dx.doi.org/10.1016/0038-092X(91)90096-F.

[2] N. Wood, Wind flow over complex terrain: A historical perspective and the prospect for large-eddy modelling, Bound.-Lay. Meteorol. 96 (1–2) (2000) 11–32, http://dx.doi.org/10.1023/A:1002017732694.

[3] J.M.L.M. Palma, F.A. Castro, L.F. Ribeiro, A.H. Rodrigues, A.P. Pinto, Linear and nonlinear models in wind resource assessment and wind turbine micro-siting in complex terrain, J. Wind Eng. Ind. Aerodyn. 96 (12) (2008) 2308–2326, http://dx.doi.org/10.1016/j.jweia.2008.03.012.

[4] B. Conan, J. van Beeck, S. Aubrun, Sand erosion technique applied to wind resource assessment, J. Wind Eng. Ind. Aerodyn. 104–106 (2012) 322–329, http://dx.doi.org/10.1016/j.jweia.2012.03.017.

[5] E.F. Bradley, An experimental study of the profiles of wind speed, shearing stress and turbulence at the crest of a large hill, Q. J. R. Meteorol. Soc. 106 (447) (1980) 101–123, http://dx.doi.org/10.1002/qj.49710644708.

[6] P.A. Coppin, E.F. Bradley, J.J. Finnigan, Measurements of flow over an elongated ridge and its thermal stability dependence: The mean field, Bound.-Lay. Meteorol. 69 (1–2) (1994) 173–199, http://dx.doi.org/10.1007/BF00713302.

[7] C. Li, S. Zhou, Y. Xiao, Q. Huang, L. Li, P.W. Chan, Effects of inflow conditions on mountainous/urban wind environment simulation, Build. Simul. 10 (4) (2017) 573–588, http://dx.doi.org/10.1007/s12273-017-0348-1.

[8] H.G. Kim, V.C. Patel, C.M. Lee, Numerical simulation of wind flow over hilly terrain, J. Wind Eng. Ind. Aerodyn. 87 (1) (2000) 45–60, http://dx.doi.org/10.1016/S0167-6105(00)00014-3.

[9] L. Enger, Simulation of dispersion in moderately complex terrain-Part A. The fluid dynamic model, Atmos. Environ. A 24 (9) (1990) 2431–2446, http://dx.doi.org/10.1016/0960-1686(90)90336-L.

[10] P. Dawson, D.E. Stock, B. Lamb, The numerical simulation of airflow and dispersion in three-dimensional atmospheric recirculation zones, J. Appl. Meteorol. 30 (7) (1991) 1005–1024, (1988-2005).

[11] L. Enger, D. Koračin, Simulations of dispersion in complex terrain using a higher-order closure model, Atmos. Environ. 29 (18) (1995) 2449–2465, http://dx.doi.org/10.1016/1352-2310(95)00160-Z.

[12] D.D. Apsley, I.P. Castro, Flow and dispersion over hills: Comparison between numerical predictions and experimental data, J. Wind Eng. Ind. Aerodyn. 67–68 (1997) 375–386, http://dx.doi.org/10.1016/S0167-6105(97)00087-1.

[13] D.D. Apsley, I.P. Castro, Numerical modelling of flow and dispersion around cinder cone butte, Atmos. Environ. 31 (7) (1997) 1059–1071, http://dx.doi.org/10.1016/S1352-2310(96)00213-0.

[14] R. Ohba, T. Hara, S. Nakamura, Y. Ohya, T. Uchida, Gas diffusion over an isolated hill under neutral, stable and unstable conditions, Atmos. Environ. 36 (36–37) (2002) 5697–5707, http://dx.doi.org/10.1016/S1352-2310(02)00642-8.
[15] P. Taylor, R.J.J. Lee, Simple guidelines for estimating wind speed variations due to small scale topographic features, Climatol. Bull. 18 (2) (1984) 3–32.
[16] G.J. Jenkins, P.J. Mason, W.H. Moores, R.I. Sykes, Measurements of the flow structure around Ailsa Craig, a steep, three-dimensional, isolated hill, Q. J. R. Meteorol. Soc. 107 (454) (1981) 833–851, http://dx.doi.org/10.1256/smsqj.45405.
[17] L.M.S. Paiva, G.C.R. Bodstein, W.F. Menezes, Numerical simulation of atmospheric boundary layer flow over isolated and vegetated hills using RAMS, J. Wind Eng. Ind. Aerodyn. 97 (9–10) (2009) 439–454, http://dx.doi.org/10.1016/j.jweia.2009.07.006.
[18] B. Blocken, A. van der Hout, J. Dekker, O. Weiler, CFD simulation of wind flow over natural complex terrain: Case study with validation by field measurements for Ria de Ferrol, Galicia, Spain, J. Wind Eng. Ind. Aerodyn. 147 (2015) 43–57, http://dx.doi.org/10.1016/j.jweia.2015.09.007.
[19] P.A. Taylor, J.L. Walmsley, J.R. Salmon, A simple model of neutrally stratified boundary-layer flow over real terrain incorporating wavenumber-dependent scaling, Bound.-Lay. Meteorol. 26 (2) (1983) 169–189, http://dx.doi.org/10.1007/BF00121541.
[20] P.J. Mason, J.C. King, Measurements and predictions of flow and turbulence over an isolated hill of moderate slope, Q. J. R. Meteorol. Soc. 111 (464) (1985) 617–640, http://dx.doi.org/10.1002/qj.49711146418.
[21] P.A. Taylor, P.J. Mason, E.F. Bradley, Boundary-layer flow over low hills, Bound.-Lay. Meteorol. 39 (1–2) (1987) 107–132, http://dx.doi.org/10.1007/BF00121870.
[22] T.F. Lavery, A. Bass, D.G. Strimaitis, A. Venkatram, B.R. Green, EPA Complex Terrain Model Development: First Milestone Report 1981, Technical report, United States Environmental Protection Agency, Washington, D.C., EPA/600/3-82/036, 1981.
[23] W. Ryan, B. Lamb, E. Robinson, An atmospheric tracer investigation of transport and diffusion around a large, isolated hill, Atmos. Environ. 18 (10) (1984) 2003–2021, http://dx.doi.org/10.1016/0004-6981(84)90186-0.
[24] J.M. Prospathopoulos, E.S. Politis, P.K. Chaviaropoulos, Application of a 3D RANS solver on the complex hill of bolund and assessment of the wind flow predictions, J. Wind Eng. Ind. Aerodyn. 107–108 (2012) 149–159, http://dx.doi.org/10.1016/j.jweia.2012.04.011.
[25] A. Bechmann, J. Berg, M. Courtney, H. Jorgensen, J. Mann, N. Sørensen, The Bolund Experiment: Overview and Background, Technical Report Risø-R-1658(EN), Riso DTU National Laboratory for Sustainable Energy, 2009, pp. 1–50.
[26] J. Berg, J. Mann, A. Bechmann, M.S. Courtney, H.E. Jørgensen, The bolund experiment, Part I: Flow over a steep, three-dimensional hill, Bound.-Lay. Meteorol. 141 (2) (2011) 219–243, http://dx.doi.org/10.1007/s10546-011-9636-y.
[27] J. Mann, N. Angelou, J. Arnqvist, D. Callies, E. Cantero, R. Chávez Arroyo, M. Courtney, J. Cuxart, E. Dellwik, J. Gottschall, S. Ivanell, P. Kühn, G. Lea, J.C. Matos, J.M.L.M. Palma, L. Pauscher, A. Peña, J. Sanz Rodrigo, S. Söderberg, N. Vasiljevic, C. Veiga Rodrigues, Complex terrain experiments in the New EuropeanWind Atlas, Phil. Trans. R. Soc. A 375 (2091) (2017) http://dx.doi.org/10.1098/rsta.2016.0101.
[28] L.H. Khurshudyan, W.H. Snyder, I.V. Nekrasov, Flow and Dispersion of Pollutants over 2-Dimensional Hills, Technical Report EPA-600/4-81-067, U.S. Environmental Protection Agency, 1981.
[29] R.E. Britter, J.C.R. Hunt, K.J. Richards, Air flow over a twodimensional hill: Studies of velocity speedup, roughness effects and turbulence, Q. J. R. Meteorol. Soc. 107 (451) (1981) 91–110, http://dx.doi.org/10.1002/qj.49710745106.
[30] W. Tian, A. Ozbay, H. Hu, Terrain effects on characteristics of surface wind and wind turbine wakes, Procedia Eng. 126 (2015) 542–548, http://dx.doi.org/10.1016/j.proeng.2015.11.302.
[31] W. Gong, P.A. Taylor, A. Dörnbrack, Turbulent boundary-layer flow over fixed aerodynamically rough two-dimensional sinusoidal waves, J. Fluid Mech. 312 (1996) 1–37, http://dx.doi.org/10.1017/S0022112096001905.
[32] K.W. Ayotte, D.E. Hughes, Observations of boundary-layer wind-tunnel flow over isolated ridges of varying steepness and roughness, Bound.-Lay. Meteorol. 112 (3) (2004) 525–556, http://dx.doi.org/10.1023/b:boun.0000030663.13477.51.
[33] H.W. Teunissen, M.E. Shokr, A.J. Bowen, C.J. Wood, D.W.R. Green, The Askervein hill project: Wind-tunnel simulations at three length scales, Bound.-Lay. Meteorol. 40 (1–2) (1987) 1–29, http://dx.doi.org/10.1007/BF00140067.
[34] B. Conan, A. Chaudhari, S. Aubrun, J. van Beeck, J. Hämäläinen, A. Hellsten, Experimental and numerical modelling of flow over complex terrain: The bolund hill, Bound.-Lay. Meteorol. 158 (2) (2016) 183–208, http://dx.doi.org/10.1007/s10546-015-0082-0.
[35] P.S. Jackson, J.C.R. Hunt, Turbulent wind flow over a low hill, Q. J. R. Meteorol. Soc. 101 (430) (1975) 929–955, http://dx.doi.org/10.1002/qj.49710143015.
[36] K.W. Ayotte, Computational modelling for wind energy assessment, J. Wind Eng. Ind. Aerodyn. 96 (10–11) (2008) 1571–1590, http://dx.doi.org/10.1016/j.jweia.2008.02.002.
[37] A.J. Bowen, N.G. Mortensen, WAsP Prediction Errors Due to Site Orography, Technical report, Technical University of Denmark, DTU Wind Energy, Roskilde, Denmark, 2004.
[38] A.F. Gomes Da Silva, A. Peña, A.N. Hahmann, E.L. Zaparoli, Evaluation of two microscale flow models through two wind climate generalization procedures using observations from seven masts at a complex site in Brazil, J. Renew. Sustain. Energy 10 (5) (2018) 053306, http://dx.doi.org/10.1063/1.5027692.
[39] A. Bechmann, N. Sørensen, J. Berg, J. Mann, P.E. Réthoré, The bolund experiment, Part II: Blind comparison of microscale flow models, Bound.-Lay. Meteorol. 141 (2) (2011) 245–271, http://dx.doi.org/10.1007/s10546-011-9637-x.
[40] A. Rasouli, H. Hangan, Microscale computational fluid dynamics simulation for wind mapping over complex topographic terrains, J. Sol. Energy Eng. 135 (4) (2013) 041005, http://dx.doi.org/10.1115/1.4024124.
[41] F.E. Hewer, Non-linear numerical model predictions of flow over an isolated hill of moderate slope, Bound.-Lay. Meteorol. 87 (3) (1998) 381–408, http://dx.doi.org/10.1023/A:1000944817965.
[42] F.A. Castro, J.M.L.M. Palma, A.S. Lopes, Simulation of the askervein flow. Part 1: Reynolds averaged Navier–Stokes equations (k - ϵ turbulence model), Bound.-Lay. Meteorol. 107 (3) (2003) 501–530, http://dx.doi.org/10.1023/A:1022818327584.

[43] J. Prospathopoulos, E.S. Politis, Evaluating Wake Models for Use in Complex Terrain, Centre for Renewable Energy Sources, 2008, pp. 83–136.
[44] A. Makridis, Modelling of Wind Turbine Wakes in Complex Terrain using Computational Fluid Dynamics (Ph.D. thesis), University of Edinburgh, 2012.
[45] A. El Kasmi, C. Masson, Turbulence modeling of atmospheric boundary layer flow over complex terrain: a comparison of models at wind tunnel and full scale, Wind Energy 13 (8) (2010) 689–704, http://dx.doi.org/10.1002/we.390.
[46] A. Chaudhari, Large-Eddy Simulation of Wind Flows over Complex Terrains for Wind Energy Applications (Ph.D. thesis), Lappeenranta University of Technology, 2014, p. 112.
[47] P.K. Sharma, V. Warudkar, S. Ahmed, Numerical and experimental analysis of the flow over sinusoidal hills, Int. J. Ambient Energy (2018) http://dx.doi.org/10.1080/01430750.2018.1542622.
[48] D. Cavar, P.-E. Réthoré, A. Bechmann, N.N. Sørensen, B. Martinez, F. Zahle, J. Berg, M.C. Kelly, Comparison of OpenFOAM and EllipSys3D for neutral atmospheric flow over complex terrain, Wind Energy Sci. 1 (1) (2016) 55–70, http://dx.doi.org/10.5194/wes-1-55-2016.
[49] M.J. Churchfield, S. Lee, P.J. Moriarty, Adding complex terrain and stable atmospheric condition capability to the OpenFOAM-based flow solver of the simulator for on/offshore wind farm applications (SOWFA), in: W. Medjroubi, B. Stoevesand, C. Peralta (Eds.), in: ITM Web of Conferences, vol. 2, (September) 2014, p. 02001, http://dx.doi.org/10.1051/itmconf/20140202001.
[50] F. Wan, F. Porté-Agel, R. Stoll, Evaluation of dynamic subgrid-scale models in large-eddy simulations of neutral turbulent flow over a two-dimensional sinusoidal hill, Atmos. Environ. 41 (13) (2007) 2719–2728, http://dx.doi.org/10.1016/j.atmosenv.2006.11.054.
[51] G. Kirkil, J. Mirocha, E. Bou-Zeid, F.K. Chow, B. Kosović, Implementation and evaluation of dynamic subfilter-scale stress models for large-eddy simulation using WRF*, Mon. Weather Rev. 140 (1) (2012) 266–284, http://dx.doi.org/10.1175/mwr-d-11-00037.1.
[52] O. Temel, L. Bricteux, J. van Beeck, Coupled WRF-OpenFOAM study of wind flow over complex terrain, J. Wind Eng. Ind. Aerodyn. 174 (November 2017) (2018) 152–169, http://dx.doi.org/10.1016/j.jweia.2018.01.002.
[53] A. Silva Lopes, J.M.L.M. Palma, F.A. Castro, Simulation of the askervein flow. Part 2: Large-eddy simulations, Bound.-Lay. Meteorol. 125 (1) (2007) 85–108, http://dx.doi.org/10.1007/s10546-007-9195-4.
[54] J. Berg, N. Troldborg, N.N.N. Sørensen, E.G. Patton, P.P. Sullivan, Large-eddy simulation of turbine wake in complex terrain, J. Phys. Conf. Ser. 854 (1) (2017) 12003, http://dx.doi.org/10.1088/1742-6596/854/1/012003.
[55] J. Berg, N. Troldborg, R. Menke, E.G. Patton, P.P. Sullivan, J. Mann, N.N. Sørensen, Flow in complex terrain - a large eddy simulation comparison study, J. Phys. Conf. Ser. 1037 (7) (2018) 072015, http://dx.doi.org/10.1088/1742-6596/1037/7/072015.
[56] Y. Han, M. Stoellinger, J. Naughton, Large eddy simulation for atmospheric boundary layer flow over flat and complex terrains, J. Phys. Conf. Ser. 753 (3) (2016) 032044, http://dx.doi.org/10.1088/1742-6596/753/3/032044.
[57] R.J.A.M. Stevens, D.F. Gayme, C. Meneveau, Large eddy simulation studies of the effects of alignment and wind farm length, J. Renew. Sustain. Energy 6 (2) (2014) http://dx.doi.org/10.1063/1.4869568.
[58] W. Munters, C. Meneveau, J. Meyers, Turbulent inflow precursor method with time-varying direction for large-eddy simulations and applications to wind farms, Bound.-Lay. Meteorol. 159 (2) (2016) 305–328, http://dx.doi.org/10.1007/s10546-016-0127-z.
[59] M.H. Baba-Ahmadi, G. Tabor, Inlet conditions for LES using mapping and feedback control, Comput. & Fluids 38 (6) (2009) 1299–1311, http://dx.doi.org/10.1016/j.compfluid.2009.02.001.
[60] T.A. Helgedagsrud, Y. Bazilevs, K.M. Mathisen, J. Yan, O.A. Øseth, Modeling and simulation of bridge-section buffeting response in turbulent flow, Math. Models Methods Appl. Sci. 29 (05) (2019) 939–966, http://dx.doi.org/10.1142/S0218202519410045.
[61] G.R. Tabor, M.H. Baba-Ahmadi, Inlet conditions for large eddy simulation: A review, Comput. & Fluids 39 (4) (2010) 553–567, http://dx.doi.org/10.1016/j.compfluid.2009.10.007.
[62] T.S. Lund, X. Wu, K.D. Squires, Generation of turbulent inflow data for spatially-developing boundary layer simulations, J. Comput. Phys. 140 (2) (1998) 233–258, http://dx.doi.org/10.1006/jcph.1998.5882.
[63] A. Ferrante, S.E. Elghobashi, A robust method for generating inflow conditions for direct simulations of spatially-developing turbulent boundary layers, J. Comput. Phys. 198 (1) (2004) 372–387, http://dx.doi.org/10.1016/j.jcp.2004.01.016.
[64] Y. Bazilevs, V.M. Calo, J.A. Cottrell, T.J.R. Hughes, A. Reali, G. Scovazzi, Variational multiscale residual-based turbulence modeling for large eddy simulation of incompressible flows, Comput. Methods Appl. Mech. Engrg. 197 (1–4) (2007) 173–201, http://dx.doi.org/10.1016/j.cma.2007.07.016.
[65] T.J.R. Hughes, G.R. Feijóo, L. Mazzei, J.-B. Quincy, The variational multiscale method-a paradigm for computational mechanics, Comput. Methods Appl. Mech. Engrg. 166 (1–2) (1998) 3–24, http://dx.doi.org/10.1016/S0045-7825(98)00079-6.
[66] T.J.R. Hughes, L. Mazzei, K.E. Jansen, Large eddy simulation and the variational multiscale method, Comput. Vis. Sci. 3 (2000) 47–59, http://dx.doi.org/10.1007/s007910050051.
[67] Y. Bazilevs, T.J.R. Hughes, Weak imposition of Dirichlet boundary conditions in fluid mechanics, Comput. & Fluids 36 (1) (2007) 12–26, http://dx.doi.org/10.1016/j.compfluid.2005.07.012.
[68] T.J.R. Hughes, J.A. Cottrell, Y. Bazilevs, Isogeometric analysis: CAD, finite elements, NURBS, exact geometry and mesh refinement, Comput. Methods Appl. Mech. Engrg. 194 (39–41) (2005) 4135–4195, http://dx.doi.org/10.1016/j.cma.2004.10.008.
[69] K. Takizawa, T.E. Tezduyar, S. McIntyre, N. Kostov, R. Kolesar, C. Habluetzel, Space–time VMS computation of wind-turbine rotor and tower aerodynamics, Comput. Mech. 53 (2014) 1–15, http://dx.doi.org/10.1007/s00466-013-0888-x.
[70] K. Takizawa, Y. Bazilevs, T.E. Tezduyar, M.-C. Hsu, O. Øiseth, K.M. Mathisen, N. Kostov, S. McIntyre, Engineering analysis and design with ALE-VMS and space–time methods, Arch. Comput. Methods Eng. 21 (2014) 481–508, http://dx.doi.org/10.1007/s11831-014-9113-0.
[71] K. Takizawa, Computational engineering analysis with the new-generation space–time methods, Comput. Mech. 54 (2014) 193–211, http://dx.doi.org/10.1007/s00466-014-0999-z.

[72] Y. Bazilevs, K. Takizawa, T.E. Tezduyar, M.-C. Hsu, N. Kostov, S. McIntyre, Aerodynamic and FSI analysis of wind turbines with the ALE-VMS and ST-VMS methods, Arch. Comput. Methods Eng. 21 (2014) 359–398, http://dx.doi.org/10.1007/s11831-014-9119-7.
[73] Y. Bazilevs, M.-C. Hsu, M.A. Scott, Isogeometric fluid–structure interaction analysis with emphasis on non-matching discretizations, and with application to wind turbines, Comput. Methods Appl. Mech. Engrg. 249–252 (2012) 28–41.
[74] M.-C. Hsu, I. Akkerman, Y. Bazilevs, Finite element simulation of wind turbine aerodynamics: Validation study using NREL phase VI experiment, Wind Energy 17 (2014) 461–481.
[75] A. Korobenko, M.-C. Hsu, I. Akkerman, J. Tippmann, Y. Bazilevs, Structural mechanics modeling and FSI simulation of wind turbines, Math. Models Methods Appl. Sci. 23 (2013) 249–272.
[76] Y. Bazilevs, A. Korobenko, X. Deng, J. Yan, Novel structural modeling and mesh moving techniques for advanced FSI simulation of wind turbines, Internat. J. Numer. Methods Engrg. 102 (2015) 766–783, http://dx.doi.org/10.1002/nme.4738.
[77] A. Korobenko, Y. Bazilevs, K. Takizawa, T.E. Tezduyar, Computer modeling of wind turbines: 1. ALE-VMS and ST-VMS aerodynamic and FSI analysis, Arch. Comput. Methods Eng. 26 (2019) 1059–1099, http://dx.doi.org/10.1007/s11831-018-9292-1.
[78] A. Korobenko, M.-C. Hsu, I. Akkerman, Y. Bazilevs, Aerodynamic simulation of vertical-axis wind turbines, J. Appl. Mech. 81 (2013) 021011, http://dx.doi.org/10.1115/1.4024415.
[79] Y. Bazilevs, A. Korobenko, X. Deng, J. Yan, M. Kinzel, J.O. Dabiri, FSI modeling of vertical-axis wind turbines, J. Appl. Mech. 81 (2014) 081006, http://dx.doi.org/10.1115/1.4027466.
[80] J. Yan, A. Korobenko, X. Deng, Y. Bazilevs, Computational free-surface fluid–structure interaction with application to floating offshore wind turbines, Comput. & Fluids 141 (2016) 155–174, http://dx.doi.org/10.1016/j.compfluid.2016.03.008.
[81] Y. Bazilevs, A. Korobenko, J. Yan, A. Pal, S.M.I. Gohari, S. Sarkar, ALE–VMS formulation for stratified turbulent incompressible flows with applications, Math. Models Methods Appl. Sci. 25 (2015) 2349–2375, http://dx.doi.org/10.1142/S0218202515400114.
[82] A. Korobenko, J. Yan, S.M.I. Gohari, S. Sarkar, Y. Bazilevs, FSI simulation of two back-to-back wind turbines in atmospheric boundary layer flow, Comput. & Fluids 158 (2017) 167–175, http://dx.doi.org/10.1016/j.compfluid.2017.05.010.
[83] M. Ravensbergen, A.M. Bayram, A. Korobenko, The actuator line method for wind turbine modelling applied in a variational multiscale framework, Comput. & Fluids 201 (2020) 104465, http://dx.doi.org/10.1016/j.compfluid.2020.104465, Available online.
[84] T.A. Helgedagsrud, Y. Bazilevs, K.M. Mathisen, O.A. Oiseth, Computational and experimental investigation of free vibration and flutter of bridge decks, Comput. Mech. (2018) http://dx.doi.org/10.1007/s00466-018-1587-4, Published online.
[85] T.A. Helgedagsrud, Y. Bazilevs, A. Korobenko, K.M. Mathisen, O.A. Oiseth, Using ALE-VMS to compute aerodynamic derivatives of bridge sections, Comput. & Fluids (2018) http://dx.doi.org/10.1016/j.compfluid.2018.04.037, Published online.
[86] J. Yan, A. Korobenko, A.E. Tejada-Martinez, R. Golshan, Y. Bazilevs, A new variational multiscale formulation for stratified incompressible turbulent flows, Comput. & Fluids 158 (2017) 150–156, http://dx.doi.org/10.1016/j.compfluid.2016.12.004.
[87] S. Xu, N. Liu, J. Yan, Residual-based variational multi-scale modeling for particle-laden gravity currents over flat and triangular wavy terrains, Comput. & Fluids 188 (2019) 114–124, http://dx.doi.org/10.1016/j.compfluid.2019.05.008.
[88] S. Xu, B. Gao, M.-C. Hsu, B. Ganapathysubramanian, A residual-based variational multiscale method with weak imposition of boundary conditions for buoyancy-driven flows, Comput. Methods Appl. Mech. Engrg. 352 (2019) 345–368.
[89] J. Yan, X. Deng, A. Korobenko, Y. Bazilevs, Free-surface flow modeling and simulation of horizontal-axis tidal-stream turbines, Comput. & Fluids 158 (2017) 157–166, http://dx.doi.org/10.1016/j.compfluid.2016.06.016.
[90] Q. Zhu, J. Yan, A moving-domain CFD solver in fenics with applications to tidal turbine simulations in turbulent flows, Comput. Math. Appl. (2019) http://dx.doi.org/10.1016/j.camwa.2019.07.034, published online.
[91] A.M. Bayram, C. Bear, M. Bear, A. Korobenko, Performance analysis of two vertical-axis hydrokinetic turbines using variational multiscale method, Comput. & Fluids 200 (2020) 104432, http://dx.doi.org/10.1016/j.compfluid.2020.104432, Available online.
[92] A.M. Bayram, A. Korobenko, Variational multiscale framework for cavitating flows, Comput. Mech. (2020) http://dx.doi.org/10.1007/s00466-020-01840-2, Available online.
[93] B. Augier, J. Yan, A. Korobenko, J. Czarnowski, G. Ketterman, Y. Bazilevs, Experimental and numerical FSI study of compliant hydrofoils, Comput. Mech. 55 (2015) 1079–1090, http://dx.doi.org/10.1007/s00466-014-1090-5.
[94] J. Yan, B. Augier, A. Korobenko, J. Czarnowski, G. Ketterman, Y. Bazilevs, FSI modeling of a propulsion system based on compliant hydrofoils in a tandem configuration, Comput. & Fluids 141 (2016) 201–211, http://dx.doi.org/10.1016/j.compfluid.2015.07.013.
[95] K. Takizawa, T.E. Tezduyar, N. Kostov, Sequentially-coupled space–time FSI analysis of bio-inspired flapping-wing aerodynamics of an MAV, Comput. Mech. 54 (2014) 213–233, http://dx.doi.org/10.1007/s00466-014-0980-x.
[96] Y. Bazilevs, K. Takizawa, T.E. Tezduyar, Computational Fluid–Structure Interaction: Methods and Applications, Wiley, February 2013, http://dx.doi.org/10.1002/9781118483565.
[97] K. Takizawa, T.E. Tezduyar, A. Buscher, Space–time computational analysis of MAV flapping-wing aerodynamics with wing clapping, Comput. Mech. 55 (2015) 1131–1141, http://dx.doi.org/10.1007/s00466-014-1095-0.
[98] K. Takizawa, T.E. Tezduyar, Y. Otoguro, T. Terahara, T. Kuraishi, H. Hattori, Turbocharger flow computations with the space–time Isogeometric analysis (ST-IGA), Comput. & Fluids 142 (2017) 15–20, http://dx.doi.org/10.1016/j.compfluid.2016.02.021.
[99] Y. Otoguro, K. Takizawa, T.E. Tezduyar, Space–time VMS computational flow analysis with isogeometric discretization and a general-purpose NURBS mesh generation method, Comput. & Fluids 158 (2017) 189–200, http://dx.doi.org/10.1016/j.compfluid.2017.04.017.
[100] Y. Otoguro, K. Takizawa, T.E. Tezduyar, K. Nagaoka, S. Mei, Turbocharger turbine and exhaust manifold flow computation with the space–time variational multiscale method and isogeometric analysis, Comput. & Fluids 179 (2019) 764–776, http://dx.doi.org/10.1016/j.compfluid.2018.05.019.
[101] T. Kanai, K. Takizawa, T.E. Tezduyar, K. Komiya, M. Kaneko, K. Hirota, M. Nohmi, T. Tsuneda, M. Kawai, M. Isono, Methods for computation of flow-driven string dynamics in a pump and residence time, Math. Models Methods Appl. Sci. 29 (2019) 839–870, http://dx.doi.org/10.1142/S021820251941001X.

[102] Y. Otoguro, K. Takizawa, T.E. Tezduyar, K. Nagaoka, R. Avsar, Y. Zhang, Space–time VMS flow analysis of a turbocharger turbine with isogeometric discretization: Computations with time-dependent and steady-inflow representations of the intake/exhaust cycle, Comput. Mech. 64 (2019) 1403–1419, http://dx.doi.org/10.1007/s00466-019-01722-2.
[103] K. Takizawa, T.E. Tezduyar, S. Asada, T. Kuraishi, Space–time method for flow computations with slip interfaces and topology changes (ST-SI-TC), Comput. & Fluids 141 (2016) 124–134, http://dx.doi.org/10.1016/j.compfluid.2016.05.006.
[104] T. Kuraishi, K. Takizawa, T.E. Tezduyar, Tire aerodynamics with actual tire geometry, road contact and tire deformation, Comput. Mech. 63 (2019) 1165–1185, http://dx.doi.org/10.1007/s00466-018-1642-1.
[105] T. Kuraishi, K. Takizawa, T.E. Tezduyar, Space–time isogeometric flow analysis with built-in Reynolds-equation limit, Math. Models Methods Appl. Sci. 29 (2019) 871–904, http://dx.doi.org/10.1142/S0218202519410021.
[106] T. Kuraishi, K. Takizawa, T.E. Tezduyar, Space–time computational analysis of tire aerodynamics with actual geometry, road contact, tire deformation, road roughness and fluid film, Comput. Mech. (2019) http://dx.doi.org/10.1007/s00466-019-01746-8, published online.
[107] K. Takizawa, T.E. Tezduyar, T. Kuraishi, Multiscale ST methods for thermo-fluid analysis of a ground vehicle and its tires, Math. Models Methods Appl. Sci. 25 (2015) 2227–2255, http://dx.doi.org/10.1142/S0218202515400072.
[108] K. Takizawa, T.E. Tezduyar, T. Kuraishi, S. Tabata, H. Takagi, Computational thermo-fluid analysis of a disk brake, Comput. Mech. 57 (2016) 965–977, http://dx.doi.org/10.1007/s00466-016-1272-4.
[109] K. Takizawa, T.E. Tezduyar, T. Terahara, Ram-air parachute structural and fluid mechanics computations with the space–time isogeometric analysis (ST-IGA), Comput. & Fluids 141 (2016) 191–200, http://dx.doi.org/10.1016/j.compfluid.2016.05.027.
[110] K. Takizawa, T.E. Tezduyar, T. Kanai, Porosity models and computational methods for compressible-flow aerodynamics of parachutes with geometric porosity, Math. Models Methods Appl. Sci. 27 (2017) 771–806, http://dx.doi.org/10.1142/S0218202517500166.
[111] T. Kanai, K. Takizawa, T.E. Tezduyar, T. Tanaka, A. Hartmann, Compressible-flow geometric-porosity modeling and spacecraft parachute computation with isogeometric discretization, Comput. Mech. 63 (2019) 301–321, http://dx.doi.org/10.1007/s00466-018-1595-4.
[112] Y. Bazilevs, V.M. Calo, Y. Zhang, T.J.R. Hughes, Isogeometric fluid–structure interaction analysis with applications to arterial blood flow, Comput. Mech. 38 (2006) 310–322.
[113] Y. Bazilevs, V.M. Calo, T.J.R. Hughes, Y. Zhang, Isogeometric fluid–structure interaction: theory, algorithms, and computations, Comput. Mech. 43 (2008) 3–37.
[114] Y. Bazilevs, J.R. Gohean, T.J.R. Hughes, R.D. Moser, Y. Zhang, Patient-specific isogeometric fluid–structure interaction analysis of thoracic aortic blood flow due to implantation of the Jarvik 2000 left ventricular assist device, Comput. Methods Appl. Mech. Engrg. 198 (2009) 3534–3550.
[115] Y. Bazilevs, M.-C. Hsu, Y. Zhang, W. Wang, T. Kvamsdal, S. Hentschel, J. Isaksen, Computational fluid–structure interaction: Methods and application to cerebral aneurysms, Biomech. Model. Mechanobiol. 9 (2010) 481–498.
[116] K. Takizawa, Y. Bazilevs, T.E. Tezduyar, C.C. Long, A.L. Marsden, K. Schjodt, ST and ALE-VMS methods for patient-specific cardiovascular fluid mechanics modeling, Math. Models Methods Appl. Sci. 24 (2014) 2437–2486, http://dx.doi.org/10.1142/S0218202514500250.
[117] K. Takizawa, Y. Bazilevs, T.E. Tezduyar, M.-C. Hsu, Computational cardiovascular flow analysis with the variational multiscale methods, J. Adv. Eng. Comput. 3 (2019) 366–405, http://dx.doi.org/10.25073/jaec.201932.245.
[118] K. Takizawa, T.E. Tezduyar, A. Buscher, S. Asada, Space–time fluid mechanics computation of heart valve models, Comput. Mech. 54 (2014) 973–986, http://dx.doi.org/10.1007/s00466-014-1046-9.
[119] K. Takizawa, T.E. Tezduyar, T. Terahara, T. Sasaki, Heart valve flow computation with the integrated space–time VMS, slip Interface, topology change and Isogeometric discretization methods, Comput. & Fluids 158 (2017) 176–188, http://dx.doi.org/10.1016/j.compfluid.2016.11.012.
[120] Y. Yu, Y.J. Zhang, K. Takizawa, T.E. Tezduyar, T. Sasaki, Anatomically realistic lumen motion representation in patient-specific space–time isogeometric flow analysis of coronary arteries with time-dependent medical-image data, Comput. Mech. (October 2019) http://dx.doi.org/10.1007/s00466-019-01774-4, published online.
[121] D. Kamensky, J.A. Evans, M.-C. Hsu, Y. Bazilevs, Projection-based stabilization of interface Lagrange multipliers in immersogeometric fluid–thin structure interaction analysis, with application to heart valve modeling, Comput. Math. Appl. 74 (9) (2017) 2068–2088.
[122] T. Terahara, K. Takizawa, T.E. Tezduyar, Y. Bazilevs, M.-C. Hsu, Heart valve isogeometric sequentially-coupled FSI analysis with the space–time topology change method, Comput. Mech. 65 (2020) 1167–1187, http://dx.doi.org/10.1007/s00466-019-01813-0.
[123] T. Terahara, K. Takizawa, T.E. Tezduyar, A. Tsushima, K. Shiozaki, Ventricle-valve-aorta flow analysis with the space–time Isogeometric discretization and topology change, Comput. Mech. 65 (2020) 1343–1363, http://dx.doi.org/10.1007/s00466-020-01822-4.
[124] C.C. Long, A.L. Marsden, Y. Bazilevs, Shape optimization of pulsatile ventricular assist devices using FSI to minimize thrombotic risk, Comput. Mech. 54 (2014) 921–932, http://dx.doi.org/10.1007/s00466-013-0967-z.
[125] M.-C. Hsu, D. Kamensky, Y. Bazilevs, M.S. Sacks, T.J.R. Hughes, Fluid–structure interaction analysis of bioprosthetic heart valves: significance of arterial wall deformation, Comput. Mech. 54 (2014) 1055–1071, http://dx.doi.org/10.1007/s00466-014-1059-4.
[126] D. Kamensky, M.-C. Hsu, D. Schillinger, J.A. Evans, A. Aggarwal, Y. Bazilevs, M.S. Sacks, T.J.R. Hughes, An immersogeometric variational framework for fluid-structure interaction: Application to bioprosthetic heart valves, Comput. Methods Appl. Mech. Engrg. 284 (2015) 1005–1053.
[127] D. Kamensky, F. Xu, C.-H. Lee, J. Yan, Y. Bazilevs, M.-C. Hsu, A contact formulation based on a volumetric potential: Application to isogeometric simulations of atrioventricular valves, Comput. Methods Appl. Mech. Engrg. 330 (2018) 522–546.
[128] C. Johnson, Numerical Solution of Partial Differential Equations By the Finite Element Method, Cambridge University Press, Sweden, 1987.
[129] A.N. Brooks, T.J.R. Hughes, Streamline upwind/Petrov-Galerkin formulations for convection dominated flows with particular emphasis on the incompressible Navier–Stokes equations, Comput. Methods Appl. Mech. Engrg. 32 (1982) 199–259.

[130] T.E. Tezduyar, Computation of moving boundaries and interfaces and stabilization parameters, Internat. J. Numer. Methods Fluids 43 (5) (2003) 555–575, http://dx.doi.org/10.1002/fld.505.
[131] K. Takizawa, T.E. Tezduyar, Y. Otoguro, Stabilization and discontinuity-capturing parameters for space–time flow computations with finite element and isogeometric discretizations, Comput. Mech. 62 (2018) 1169–1186, http://dx.doi.org/10.1007/s00466-018-1557-x.
[132] K. Takizawa, Y. Ueda, T.E. Tezduyar, A node-numbering-invariant directional length scale for simplex elements, Math. Models Methods Appl. Sci. (2019) http://dx.doi.org/10.1142/S0218202519500581, published online.
[133] Y. Otoguro, K. Takizawa, T.E. Tezduyar, Element length calculation in B-spline meshes for complex ceometries, Comput. Mech. (2019) http://dx.doi.org/10.1007/s00466-019-01809-w, published online.
[134] A. Fluids Engineering Division ASME, Procedure for estimation and reporting of uncertainty due to discretization in CFD applications, J. Fluids Eng. 130 (7) (2008) 078001, http://dx.doi.org/10.1115/1.2960953.
[135] R.D. Moser, J. Kim, N.N. Mansour, Direct numerical simulation of turbulent channel flow up to $re\tau = 590$, Phys. Fluids 11 (4) (1999) 943–945, http://dx.doi.org/10.1063/1.869966.
[136] D.B. Spalding, A single formula for the “law of the wall”, J. Appl. Mech. 7 (12) (1961) 3078.
[137] R.B. Dean, Reynolds number dependence of skin friction and other bulk flow variables in two-dimensional rectangular duct flow, J. Fluids Eng. 100 (June 1978) (1978) 215–223.
[138] M.E. Moghadam, Y. Bazilevs, T.-Y. Hsia, I.E. Vignon-Clementel, A.L. Marsden, Modeling of Congenital Hearts Alliance (MOCHA), A comparison of outlet boundary treatments for prevention of backflow divergence with relevance to blood flow simulations, Comput. Mech. 48 (2011) 277–291, http://dx.doi.org/10.1007/s00466-011-0599-0.